The Pennsylvania State University

The Graduate School

College of Engineering

A SYNERGISTIC PASSIVE AND ACTIVE SHIMMING SYSTEM TO OPTIMIZE B_0 FIELD HOMOGENEITY IN MICRO MR SPECTROSCOPY

A Dissertation in

Bioengineering

by

Rahul P. Dewal

Submitted in Partial Fulfillment

of the Requirements

for the Degree of

Doctor of Philosophy

August 2016

The dissertation of Rahul P. Dewal was reviewed and approved* by the following:

Qing X. Yang

Professor of Radiology and Neurosurgery

Dissertation Advisor

Chair of Committee

Mark D. Meadowcroft

Assistant Professor of Neurosurgery and Radiology

William J. Weiss

Professor of Surgery and Bioengineering

Nanyin Zhang

Associate Professor of Bioengineering

William O. Hancock

Professor of Bioengineering

Chair of the Intercollege Graduate Degree Program in Bioengineering

*Signatures are on file in the Graduate School

Abstract

This research presents a targeted, synergistically combined passive and active shimming system to correct for susceptibility-induced B_0 inhomogeneity artifacts in magnetic resonance (MR) imaging and spectroscopy. This system would be of great significance to researchers using MR imaging at ultra-high fields (7–14 T), where B_0 inhomogeneity artifacts are a major limiting factor for many *in vivo* applications.

At boundaries between materials of differing magnetic susceptibility, such as the air-tissue boundaries in the sinus cavities or ear canals, the differing susceptibilities of the imaged tissues can distort the applied magnetic field. These inhomogeneities can lead to local distortion and signal loss artifacts in MR images and line broadening in MR spectra. Active shimming, involving the adjustment of magnetic shim coils, is used to correct first-order inhomogeneities, but higher-order active shimming can be difficult and expensive. Instead, passive shimming may be used to correct such higher-order inhomogeneities. Passive shimming involves placing pieces of material that have high magnetic susceptibility values compared to body tissues in the vicinity of said tissues in order to perturb the magnetic field such that the inhomogeneities are corrected. Previous experiments have been performed with several passive shimming methodologies that show promising results. However, they have various drawbacks, with several lacking precision shim placement and another requiring excessive manual measurements for best results.

This research pursues precision correction of inhomogeneities via two specific aims:

Specific Aim 1: Develop numerical synergistic shim simulation and optimization software, which *simultaneously* optimizes the linear active shim gradient settings and passive shim element configuration for B_0 inhomogeneity correction of a given volume of interest (VOI).

Specific Aim 2: Develop passive shim frame hardware that implements the synergistic shimming solution.

The technique was validated in a 7T Bruker MRI system in a customized susceptibility phantom and in *in vivo* mice by using it to improve the B_0 magnetic field homogeneity and spectral water line widths from predetermined regions of interest within the mouse brain. These pilot data demonstrate the feasibility of using such a system to improve MR spectroscopy data quality. Future work could extend the technique to human applications, which would be of great benefit to human neurological studies of regions near the sinuses.

Table of Contents

List of Figures

List of Tables

Acknowledgements

This work was made possible by the support of many, many individuals. First, I would like to thank my advisor, Dr. Qing X. Yang, for his support and sage advice throughout the years. I would also like to thank my other committee members, Dr. Mark D. Meadowcroft, Dr. William J. Weiss, and Dr. Nanyin Zhang for the same.

I would also like to thank the members of the CNMRR, the Center for NMR Research, at Penn State Hershey. There are too many to name—for example, Zhipeng, for stimulating discussions, whether about work or otherwise, and being a great friend—and this applies to the rest as well. Giuseppe, for creativity and artistry, even in engineering. Chris, all of them, for having such solid knowledge and sharing it with us. Mark, for continued advice over the years and impressive skills in an impressive number of areas. Patti, for both great technical help and great cooking tips. Sebastian, for being a humble expert at everything, including life. Mike, for demonstrating grit and a willingness to open your mind. Megha, for convincing me to see a different point of view. Jeff for always keeping an eye out for everyone. Jianli and Xiaoyu, for always having great input and solid reasoning. Byeong, Sukhoon, and Yeun-chul for being my seniors and mentors. Our administrative staff, including Judy and Amanda, for keeping everything running smoothly. And, of course my advisor, for his (sometimes) personable approach and (sometimes) fascinating metaphysical interpretations. These are but a few.

Naturally, I would also like to thank my family and friends, who supported me even when I was too busy to come visit them. Mom, Dad, my brother Ninad, and the rest of my extended family. Neal, Smita, Riya, and Tanya, who happened to move into the area and whose home became mine away from home. Friends back home, S&E, the old college gang, friends around Hershey, AZ, and PP, for keeping me grounded.

This work is dedicated to my grandparents, Mr. Alan Nuccio, and Dr. Thomas Pritchard.

1 Introduction

The presence of inhomogeneities in the magnetic field poses a perpetual problem for magnetic resonance (MR) imaging and spectroscopy. In this section, the nature of these inhomogeneities, their deleterious effects on the acquired data, and standard methods of compensating for these inhomogeneities will be discussed.

1.1 Magnetic Susceptibility and Artifacts

Magnetic susceptibility (χ) is a quantitative measure of a material's tendency to interact with and distort an applied magnetic field (1). It is governed by the equation:

$$M = \chi H \qquad [1.1]$$

where H is the applied magnetic field and M is the material's induced magnetization. The resultant magnetic induction, B, representing average field of force within an object, is then given by:

$$B = \mu_0 (H + M) \qquad [1.2]$$

or, combining the two:

$$B = \mu_0 H (1 + \chi) = \mu H \qquad [1.3]$$

where μ is electromagnetic permeability and the physical constant μ_0 is the electromagnetic permeability of free space. It is this induced magnetic field, or B field, that is of relevance to MR.

The main static magnetic field within the bore of an MR magnet, the B_0 field, is designed to be as uniform, or homogeneous, as possible. When a subject is placed into the bore of an MR magnet, the subject's tissues induce additional B fields that perturb the B_0 magnetic field. At boundaries between tissues of differing susceptibilities, such as the air-tissue boundaries in the sinus cavities or ear canals, the induced inhomogeneities in the B_0 field, or ΔB_0, can lead to local distortion and signal loss artifacts in MR images (2) and line broadening in MR spectra (3) as a result of spin dephasing. An example of these image artifacts in the mouse brain is shown in Figure 1.1.

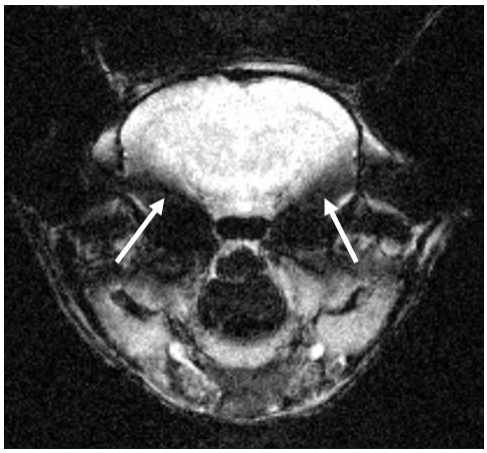

Figure 1.1. Magnetic susceptibility-induced B_0 inhomogeneity artifacts in the mouse brain. The white arrows point to regions of signal loss arising from the posterior maxillary sinuses.

In micro MR imaging (the imaging of small animals such as mice), a magnet with a high field strength (7.0 T or above) is preferred for improved SNR. However, the strength of the field inhomogeneities are directly proportional to the magnet field strength (4). Thus, the higher field strength will also increase the effects of susceptibility-induced inhomogeneities. Further, due to the relatively low volume of the mouse brain as compared to the surface area of the air-tissue interfaces in the sinuses or ear canals, the artifacts from these inhomogeneities extend far into the brain region, affecting signal from regions of scientific interest, such as the olfactory bulb or midbrain (5). Imaging of human subjects runs into similar issues in areas such as the orbitofrontal cortex (6). Therefore, methods to correct for these inhomogeneities or to reduce their effects are of great interest to researchers and clinicians.

1.1.1 ΔB Field Mapping

In order to characterize the spatial distribution of the static field inhomogeneities, various MR scanner sequences called field mapping sequences are employed. Local deviations in static magnetic field from the nominal B_0 value will cause hydrogen nuclei to have locally varying resonance frequencies according to the Larmor equation (7):

$$\omega(\vec{r}) = \gamma B(\vec{r}) \quad [1.4]$$

where γ is the gyromagnetic ratio for hydrogen nuclei, or approximately 42.58 MHz/T. When a radiofrequency (RF) pulse with a frequency ω_0 corresponding to the nominal B_0 field strength value is applied to excite the hydrogen nuclei, the nuclei's net magnetization vector will begin to precess about the B_0 direction. However, due to microscopic and macroscopic ΔB inhomogeneities, they will precess at different frequencies, leading to the nuclei precessing out of phase over time. This loss of phase coherence leads to what is known as T2* decay of the net transverse magnetization, but what is of specific concern to us is the local accumulation of relative phase differences from the on-resonance condition as per the following relation:

$$\phi(\vec{r}) = \gamma \cdot \Delta B(\vec{r}) \cdot t \quad [1.5]$$

where ΔB is the local difference in static magnetic field strength from the nominal B_0 value, and t is the amount of time elapsed since RF excitation. This spatially-varying phase accumulation can then be measured by the scanner and the ΔB spatial distribution calculated from this.

The simplest method of ΔB field mapping generally uses the difference of two echo images at different echo times (TE). The relative phase difference between the two echoes is then given by:

$$\Delta\phi(\vec{r}) = \gamma \cdot \Delta B(\vec{r}) \cdot \Delta TE \quad [1.6]$$

where ΔTE is the difference in echo times of the two images. The ΔB field values can then be calculated by solving for ΔB in Equation 1.6:

$$\Delta B(\vec{r}) = \frac{\Delta\phi(\vec{r})}{\gamma \Delta TE} \quad [1.7]$$

Thus, by acquiring two images with different echo times and computing the voxel-by-voxel phase difference between the two images, the ΔB field map can be computed.

There are a number of practical concerns. By setting the ΔTE very short (e.g., on the order of several hundred microseconds), the measured phase differences can be contained within a 2π range of phase for the expected range of ΔB inhomogeneity values. However, this will lower the signal-to-noise ratio (SNR), or precision, of the computed ΔB field map because

the range of measured phase values remains low compared to the noise floor. Additionally, this makes it impractical to acquire both echo images as part of the same multi-echo scan, which doubles the acquisition time and adds potential phase offset issues. Setting a longer ΔTE (e.g., on the order of several milliseconds) allows for acquisition using a single sequence, but introduces phase wrapping, or the aliasing of phase accumulation exceeding the 2π range. Various spatial and temporal phase unwrapping methods have been created to address this issue (8-10), and as long as the unwrapping is performed correctly, the final field map will have greater precision than a short ΔTE map. In this work, we used the Bruker FieldMap sequence, which is a standard 3D multi-echo gradient-echo imaging sequence available on the scanner console with a proprietary robust phase unwrapping algorithm built into the field map reconstruction pipeline.

1.2 Standard Inhomogeneity Correction Methods

Inhomogeneities in the magnetic field are directly compensated using standard shimming techniques. There are two major classes of shimming techniques: passive shimming and active shimming. In passive shimming, pieces of shim material are strategically placed within the B_0 field to passively alter the magnetic field. In active shimming, special shim coils built into the magnet are used to apply a magnetic field to actively cancel out the inhomogeneities.

1.2.1 Ferromagnetic Passive Shimming

Upon installation of the MR magnet, ferromagnetic passive shims are placed within the bore to compensate gross B_0 field inhomogeneities arising from magnet imperfections and the magnet's environment (11). A field probe is placed within the magnet bore to measure gross magnetic field inhomogeneities, these are input into a simulation and computation algorithm, and then thin steel shims are mounted on rails along the inside surface of the magnet bore. The

new inhomogeneity fields are measured and the shims adjusted iteratively until the field homogeneity within a spherical region around the magnet isocenter meets manufacturer specifications.

1.2.2 Spherical Harmonic Active Shimming

To compensate for localized B_0 inhomogeneities arising from subject tissue susceptibility differences, magnets are equipped with spherical harmonic active shim coils. The field inhomogeneity is decomposed into multiple orders of spherical harmonic fields: zero-order, first-order (linear), second-order, and so forth. Each active shim coil is designed to produce a static magnetic field that compensates a single spherical harmonic component of a given order of the decomposed inhomogeneity field, as shown in Table 1.1 and Figure 1.2. The currents in these active shim coils are optimized such that the sum of the magnetic fields produced negate the subject-specific inhomogeneity field. The optimization methods used to determine these shim currents vary, from basic magnet autoshimming to more precise methods such as measuring the inhomogeneity along predetermined projections (FASTMAP) or acquiring a full field map (MapShim). (12)

While active shimming is a useful tool, it has certain limitations. In general, susceptibility-induced inhomogeneities, such as those found at air-tissue interfaces in the sinuses, contain multiple orders of local field gradients and require a combination of shim settings to be compensated effectively. Standard MR magnets only come equipped with active shim coils for first-order (linear) spherical harmonic terms. Shim coils that can shim second-order spherical harmonic terms are optional and come at an additional cost, and shim coils higher than second-order are not widely available. Additionally, higher-order shim coils require higher currents, and the currents required to optimally compensate such inhomogeneities can exceed the specifications of the hardware. Therefore, it is difficult to remove the field inhomogeneities with standard active shims alone.

Table 1.1. Spherical harmonic shim field functions up to second order (3).

Name	Order (n)	Degree (m)	Function
Z	1	0	z
X	1	1	x
Y	1	−1	y
Z2	2	0	$z^2 – (x^2 + y^2) / 2$
ZX	2	1	zx
ZY	2	−1	zy
X2−Y2	2	2	$x^2 – y^2$
XY	2	−2	xy

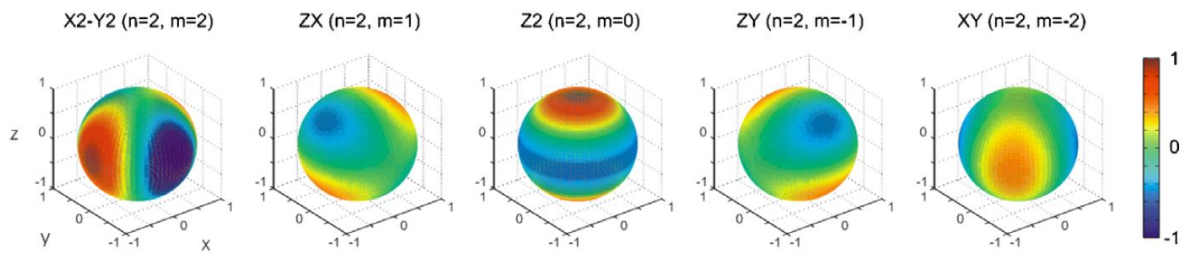

Figure 1.2. Visualization of normalized second-order spherical harmonic shim field shapes on the surface of a unit sphere. (3)

1.3 Further Inhomogeneity Correction Methods

There are several other methods for further compensating for field inhomogeneities. These include the use of tailored RF pulses, special pulse sequence design, image reconstruction methods, and postprocessing methods. For example, the GESEPI method involves acquiring the image multiple times while varying the slice select magnetic gradient and then reconstructing the final image by using a 3D Fourier transform of the sets of acquired data, resulting in lower signal loss artifacts (13). Similarly, the PLACE method acquires the image multiple times while varying the phase encoding magnetic gradient, allowing for reconstruction

of an image with less geometric distortion (14). These methods have the disadvantage of requiring extra time to acquire the image multiple times, which is especially problematic for applications that require short imaging times, such as functional MR imaging (fMRI). Postprocessing methods can use curve-fitting of multi-echo images to reduce artifacts and don't require additional acquisition time, but are unable to cope with signal loss (15,16). RF pulse tailoring can reduce artifacts and signal loss at the cost of additional acquisition and computation time (17).

One feature these methods tend to have in common is that they make simplifying assumptions about the nature and order of the background gradient across the voxel or even across the slice. If the field inhomogeneity has significant higher-order components, as is often the case near air-tissue boundaries, such methods will not be as effective.

1.3.1 Localized Passive Shimming

Localized passive shimming can potentially be used to correct these localized, higher-order inhomogeneities. Rather than using strong ferromagnetic shims, localized passive shimming tends to use much weaker, diamagnetic or paramagnetic shims placed nearby or within the subject to locally correct for subject-specific tissue-boundary-induced inhomogeneities.

Some form of theoretical calculation or simulation must be used to determine placement of the shim material and the approximate expected results. Koch specifies several simplifying assumptions that allow for the development of an elegant model: 1) far enough away from the shim material, the effects on the net magnetic field add together using linear superposition, and 2) the shim material's relatively large susceptibility value allows one to neglect the effects of the surrounding air and tissue on the material (18).

1.3.2 Magnetic Properties of Materials

Materials to be used for passive shimming can fall under one of three categories of magnetic state—paramagnetic, diamagnetic, and ferromagnetic. Paramagnetic materials are those materials that have a positive magnetic susceptibility value, from zero up to approximately 10^{-2}. Diamagnetic materials are materials with a negative magnetic susceptibility value. Lastly, ferromagnetic materials have large, positive susceptibility values. These materials strongly distort the applied magnetic field, requiring that they be used with caution nearby and within the magnet (1). However, if used judiciously, they can still be used for passive shimming (3).

The susceptibility values of both paramagnetic and diamagnetic materials are often given in parts per million (ppm), essentially equivalent to $1.0 \cdot 10^{-6}$. Air and tissue (composed mostly of water), for example, have values of approximately 0.4 ppm and −9.0 ppm, respectively, making air slightly paramagnetic and tissue slightly diamagnetic (18). An overview of the spectrum of magnetic materials is shown in Figure 1.3 below.

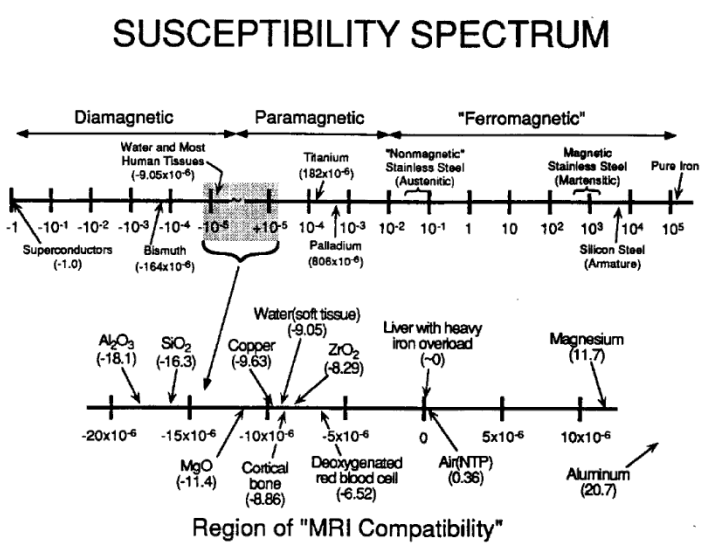

Figure 1.3. An overview of the susceptibility spectrum of magnetic materials (1).

1.3.3 Effects of Materials on the Magnetic Field Distribution

In order to make effective use of passive shimming, a way to predict the effects of a given piece of material on the B_0 magnetic field distribution is required. There exists a special case analytical solution for the external field of a homogeneous sphere of material of radius *a* with magnetic susceptibility χ centered at the origin (1):

$$\Delta B_z = \frac{\Delta\chi B_0 a^3}{3} \frac{2z^2 - x^2 - y^2}{(x^2+y^2+z^2)^{\frac{5}{2}}} \qquad [1.8]$$

The result is a field similar in shape to the standard dipole field, as shown in Figure 1.4 below.

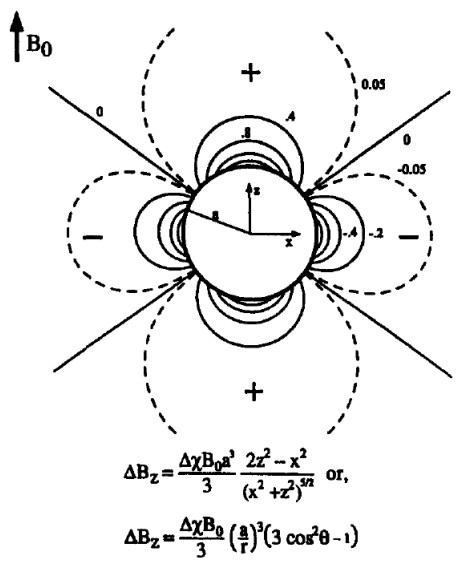

Figure 1.4. Two-dimensional diagram of the external field of a homogeneous sphere of material with magnetic susceptibility χ and radius *a* (1).

For more arbitrary distributions of material, numerical methods are generally required to calculate the field produced. A finite-difference numerical solver that calculates the magnetic field via iterative solution of Maxwell's equations is available (19). However, this method is relatively slow, requiring a computation time on the order of hours. A more recent method makes use of the Fast Fourier Transform to effectively convolve the response shown in Figure 1.4 with the magnetic susceptibility distribution to provide a one-shot, approximate calculation of the magnetic field that is much faster than the iterative method (12,20):

$$\Delta B(\vec{r}) = B_0 \cdot FT^{-1}\left\{G\left(\vec{k}\right) \cdot FT\{\chi(\vec{r})\}\right\}, \text{ where } G\left(\vec{k}\right) = \frac{1}{3} - \frac{k_z^2}{k_x^2+k_y^2+k_z^2} \quad [1.9]$$

The computation time is on the order of seconds, potentially allowing for practical use during a clinical scanning session. This research uses this Fourier Transform-based approach to simulate the effects of a piece of shim material on the B_0 static magnetic field due to its balance of speed and accuracy.

2 FT-based Synergistic Passive Shim Optimization Research Design

It has been shown that magnetic field inhomogeneities induced by susceptibility differences is a problem that affects clinicians and researchers. Specifically, second-order and higher inhomogeneities are unable to easily be canceled out by standard active shimming, special pulse sequences, or postprocessing. Passive shimming is a relatively simple, effective way to deal with these higher-order inhomogeneities. We therefore began by examining the methodology used in prior work in the field of localized passive shimming.

2.1 Existing Passive Shimming Methodologies and Limitations

Several different shim placement paradigms have been developed. For human subjects, shaped pieces of pyrolytic graphite encased in plastic molded to the subjects' mouths have been tested (21). This has the drawback of requiring the subject to hold the shimming material in their mouth, requiring special attention to hygiene and comfort. It is also not likely to be feasible in animal studies in general, let alone in MR studies of mice, due to the logistical and safety issues of placing shim material inside an anesthetized and uncooperative subject's mouth.

Another approach is to mount small pieces of shimming material in strategic locations on a frame that encircles the subject. This has the benefit of being flexible and non-intrusive. It is this model that this research will pursue. However, one of the existing methods used calculation of spherical harmonics and used pieces of permalloy, a strong ferromagnetic material, mounted on a large-radius frame far away from the subject (3). This resulted in a coarse, lower-order correction of the field homogeneity somewhat similar to the effects produced by active shimming rather than the more precise correction pursued by this research. This precision will be necessary for the correction of strong higher-order field inhomogeneities, especially for MR imaging of small animals such as mice.

Some methods do indeed use diamagnetic and paramagnetic shimming materials mounted close to the subject for a more localized B_0 correction field. However, one such method

uses experimentally measured unit shim responses as a basis for its shim design (18). This method works well for active shimming. However, for passive shimming, this has various drawbacks, such as needing to manually measure the unit shim response for each radial distance from the center of the magnet, leading to a tradeoff between practicality and flexibility. Another method does make use of the analytical solution for the external perturbation field of a sphere to avoid such drawbacks (22). However, this approach has the drawback of having inaccuracies in the simulated passive shim correction fields, leading to less optimal shimming results. Additionally, neither method attempts to synergistically work together with active shimming, as this research will do.

Finally, one method does not use passive shimming at all, but instead uses a custom set of up to 48 localized active shim coils to shim the B_0 static magnetic field (23-25). These coils are mounted on a plastic former that sits between the subject and the RF coil. This approach allows for localized field correction in a manner similar to passive shimming without the need for precision placement of passive shim elements and can provide better results than standard spherical harmonics-based active shimming due to its closer proximity to the subject and degrees of freedom granted by the numerous coils. However, this requires significant additional and costly hardware, with power supplies and amplifiers to drive each shim coil as well as a controller interface to set the specific shim currents in each coil.

2.2 Motivation and Specific Aims

For MR imaging and spectroscopy of the mouse brain, targeted and precise passive shimming is needed. This requires the ability to optimize and place shims at arbitrary positions in the magnet. To accomplish this without excessive manual measurement and labor, our technique uses a method to quickly and accurately simulate the B_0 field effects of shim elements in conjunction with an accompanying optimization algorithm. Additionally, our technique incorporates synergistic active shimming, in which the passive shims are used primarily for their

ability to cancel second-order and higher inhomogeneities while allowing the linear active shim coils to handle the first-order (linear) inhomogeneities. Improved field homogeneity is believed to be due to this specialization in which active and passive shimming each have their own separate role. This design was pursued via two concurrently-pursued specific aims with sub-aims:

Specific Aim 1: Develop numerical synergistic shim simulation and optimization software, which *simultaneously* optimizes the linear active shim gradient settings and passive shim element configuration for B_0 inhomogeneity correction of a given volume of interest (VOI).

1. Analyze the B_0 field inhomogeneity map and geometry data acquired from the subject via the MR scanner console for initial calibration.
2. Prepare the simulated shim element library for use.
3. Simultaneously optimize the linear active shim gradient settings and passive shim element configuration for minimum B_0 inhomogeneity within the specified VOI.
4. Compare the B_0 inhomogeneity before and after synergistic shimming to evaluate its efficacy.

Specific Aim 2: Develop passive shim frame hardware that implements the synergistic shimming solution.

1. Develop the shim frame used to mount the passive shim elements in the locations specified by the optimized synergistic shim solution.
2. Develop calibration procedures that ensure that the simulation space maps accurately to laboratory space.

The products of these aims will then be validated via preliminary demonstration of the application of the synergistic shimming system to phantom and *in vivo* mouse localized B_0 homogeneity improvement. The significance of this work is to demonstrate the feasibility of using the synergistic shimming method to provide a low-cost approach for improving localized B_0 homogeneity for research studies examining brain regions where shimming remains problematic.

2.3 Specific Aim 1: Develop Synergistic Shim Simulation and Optimization Software

The synergistic shim software pipeline consists of four steps: calibration, library preparation, simulation and optimization, and evaluation. These are described below, and an overview of the overall workflow pipeline is shown in Figure 2.1. All of the software components are implemented in MATLAB (The MathWorks, Inc., Natick, MA) as .m scripts.

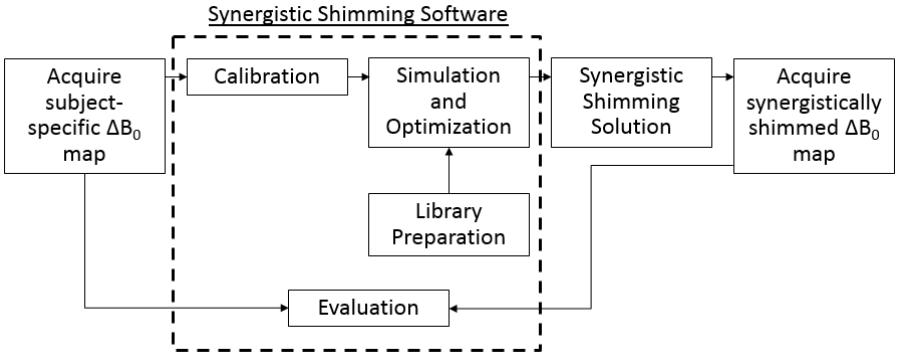

Figure 2.1. Workflow pipeline of the synergistic shimming software.

2.3.1 Initial Calibration

The software reads the acquired MR scanner data using MRIUtilMATLAB, an in-house software package developed by our lab. It then analyzes the fiducial markers (see Specific Aim 2) to ensure that the subject is not tilted and to determine the position of the shim frame with respect to the magnet isocenter. This is accomplished by fitting in cylindrical coordinates the expected fiducial marker geometry to the measured geometry and recording the differences. Finally, it exports this data for use in the following steps.

2.3.2 Library Preparation

In order to speed up the optimization for use with *in vivo* subjects, the VOI-based Fourier Transform method (26) is used to pre-calculate the B_0 perturbation fields of single passive shim elements of various sizes, positions, and magnetic susceptibility values. As the shim frame is

designed to position axially-oriented cylindrical shim elements of fixed ¼" (6.35 mm) diameter and varying heights, the parameters used to represent a single passive shim element were r, θ, z, χ, and h. The first three variables represent position in cylindrical coordinates, the next represents the material type (graphite or titanium), and the last represents the height of the cylinder. The ranges and discrete steps of these values to be pre-calculated and later used in the optimization can be configured. The values used for *in vivo* experiments are shown in Table 2.1; the total number of combinations of values, and thus stored shim fields, was 11360. Once computed, these shim fields are stored in a library that can be reused across multiple subjects. As preparation for the optimization step, this library is loaded and processed to match the current subject and chosen VOI.

Table 2.1. Value ranges pre-calculated within the library. It was found that placing shim elements as close as possible was optimal, so r was chosen to span only one value.

Variable	Minimum	Step	Maximum
r	24 mm	–	–
θ	0°	22.5°	337.5°
z	−35 mm	1 mm	35 mm
χ	−116 ppm	–	174 ppm
h	5 mm	5 mm	25 mm

2.3.3 Simulation and Optimization

In the optimization step, the optimal combination of passive shim elements and active shim coil settings for the current subject is determined via linear superposition of the individual shim fields and evaluation of the variance of the resultant shimmed ΔB_0 field. The synergistic shim combination with the lowest variance within the VOI of the subject is considered to be optimal. The flowchart of these two steps is shown in Figure 2.2.

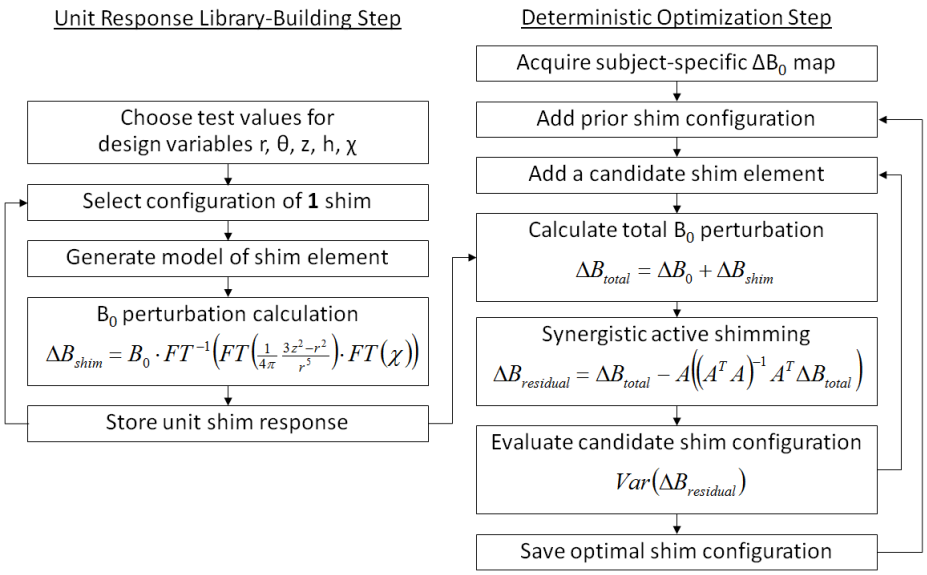

Figure 2.2. Flowchart of the simulation and optimization component of the software.

First, the ΔB_0 map obtained from the subject is input into the algorithm. For each candidate shim element in the library, the shim element is prospectively added to the total shim configuration. The effect of this shim element on the ΔB_0 field within the volume of interest (VOI) is then calculated by adding the pre-computed perturbation field generated by the shim element stored in the library to the total ΔB_0 field. The optimal first-order active shim fields are then calculated using the Moore-Penrose pseudo-inverse. These active shim fields are then applied to the passively shimmed B_0 field, resulting in synergistic passive and active shimming (27). The suitability of the prospective shim setup is then evaluated by calculating the variance of the synergistically shimmed ΔB_0 field within the VOI. A lower variance indicates a more homogeneous static magnetic field. This variance is saved for later comparison. This is then repeated for each candidate shim element in the library, and the best candidate is accepted for inclusion in the final shim configuration.

The new total ΔB_0 field is then used as a basis for the next round of optimization, and the next shim element to add to the final shim configuration is determined by once again evaluating all candidate shim elements in the library for their effect on the ΔB_0 field within the VOI. At all

steps, candidate shim configurations are checked to ensure that they are valid, i.e., that individual shim elements are not physically overlapping. In this way, additional passive shim elements are added to the configuration one by one to obtain progressively improved field homogeneity until an end condition is reached. In this case, the end condition is reached when a total of 4 passive shim elements are accepted into the shim configuration, or when it is determined that no possible passive shim element could improve the current shim configuration. This condition was chosen as a good balance of ease of practical implementation on the hardware frame and reasonably good convergence to optimal shim performance.

The final shim configuration, consisting of both passive shim element positions and linear active shim strengths, is then output to the user in an easily-readable format so that it can be implemented on the hardware frame and used to synergistically shim the VOI. It can also be displayed graphically in a 3D rendering to ensure that the user understands where to place the shims in relation to the subject.

2.3.4 Shim Evaluation

To minimize online optimization overhead time during *in vivo* experiments, a processing pipeline was developed in MATLAB that quickly compare the pre-synergistic shim VOI inhomogeneity with the computed post-shim and experimentally acquired post-shim inhomogeneities. First, the MR data is copied manually from the scanner console to the synergistic shimming workstation via File Transfer Protocol (FTP) connection over the local network. The pipeline then takes the scanner data, acquisition IDs, VOI, and passive shim configurations as inputs and reads in the ΔB_0 field maps and water peak spectra, simulates passive shim elements, and calculates simulated synergistically shimmed ΔB_0 maps. It then computes and displays ΔB_0 difference maps, histograms of the B_0 field homogeneity within the VOI, variance of the B_0 field homogeneity within the VOI, and spectroscopic water peak line widths for the various cases. These can be used to evaluate the accuracy of the implemented

synergistic shim configuration to its simulation and any improvement in field homogeneity offered by the synergistic shim solution over the standard active shim solution—both the default magnet autoshim and the localized, optimized active shim. The latter is evaluated qualitatively by visually comparing the B_0 field maps and the histograms of the ΔB_0 values of the voxels within the VOI and quantitatively by comparing the variance of the ΔB_0 values within the VOI and the water peak widths for each case. A reduced variance and narrower water peak would indicate a more homogeneous B_0 field, demonstrating that the method can successfully better shim B_0 inhomogeneities.

2.3.5 Optimization Algorithm Development and Challenges

The above design went through several iterations before arrival at its current form. Initially, an existing optimization framework package, Differential Evolution and Particle Swarm Optimization (DEPSO), was used in conjunction with a simple passive shim simulation algorithm based on the analytical solution for a homogeneous sphere of material (1) to optimize shim material placement. The framework makes use of the particle swarm optimization algorithm based on social swarm intelligence. The search space is randomly seeded with “particles”, each of which uses the simplified field solver to calculate the magnetic field distribution for the given shim material configuration represented by the particle’s location in the search space. It then uses a cost function to determine the suitability of the current shim configuration, in this case the variance of the shimmed field within the VOI. At each time step, the particles share their suitability results and incrementally move towards the best solution found thus far in the search space. The field inhomogeneity is then recalculated for each particle and the cost function re-evaluated. The result is that the particles tend to gravitate towards an optimal solution (28). However, it was found that this approach, while able to stochastically sample and search a wide search space relatively quickly, was still far too slow for *in vivo* use, or even convenient *ex vivo* use, taking on the order of hours to find a solution.

The DEPSO optimization was thus replaced with a simple numerical optimization algorithm using MATLAB's fmincon function. This uses numerical methods to find a local minimum to the provided constrained optimization problem given an initial condition. Further, since the analytical method for calculating the B_0 field perturbations of the shim elements was applicable only to spheres, the ability of this method to approximate the perturbations of the cylindrical shim elements by simulating them as spheres of equivalent volume was explored. When comparing the field perturbations of shim cylinders using the gold standard finite-difference numerical method (19) to the perturbations of the equivalent spheres using the analytical method, it was found that there could be noticeable deviations, especially if the cylinder was especially long or close to the subject to be shimmed. For this reason, it was decided to incorporate the more accurate Fourier Transform-based B_0 field perturbation calculation method (12) into the optimization algorithm.

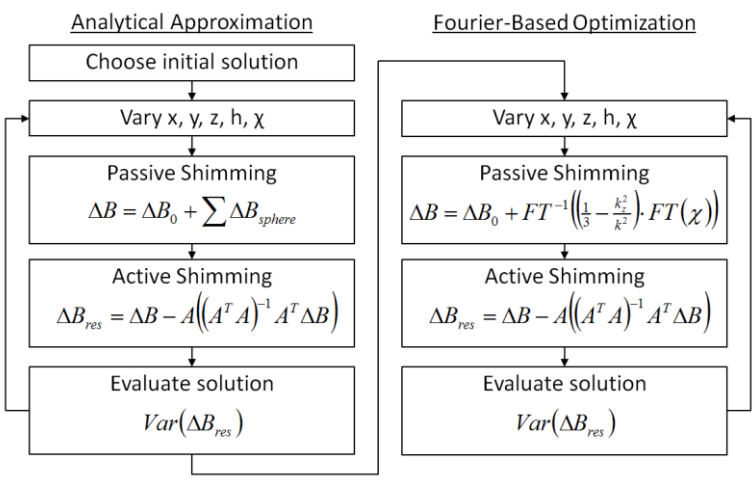

Figure 2.3. Workflow of the previous iteration of the optimization algorithm.

At this stage, the optimization method was comprised of two steps, as shown in Figure 2.3 above: 1) a fast, but approximate analytical solution-based calculation and 2) a slower, but more accurate numerical Fourier Transform-based calculation. Eight cylinders of fixed ¼" diameter and variable position, length, and susceptibility were used as the shim elements. First,

these shim elements were scattered around the sample. The effects of the shim elements on B_0 were then approximated using the analytical solution and linearly superimposed with the B_0 field in the sample. The optimal first-order active shim fields were calculated using the Moore-Penrose pseudo-inverse and then applied. The suitability of this synergistic shim setup was then evaluated by calculating the variance of the shimmed ΔB_0 field within the VOI. The locations, lengths, and susceptibility values of the cylinders were then iteratively optimized by using the MATLAB constrained numerical minimization function until a cost function convergence criterion was reached. The solution output from this round of optimization was then used as the starting point for the next round of optimization, which used the Fourier Transform-based method to calculate the B_0 field perturbation of the shim cylinders instead of the analytical solution (12). The nimble analytical approximation step thus provided, in theory, a reasonably good starting point for the slow but steady Fourier Transform-based step.

Unfortunately, this approach too had several issues. Problem conditioning, or the process of normalizing the value ranges of each of the design variables, proved necessary to avoid the optimization giving undue weight to one of the variables, and this further complicated the software design by requiring that the program keep careful track of the conditioning and unconditioning status of the passive shim configuration matrices at all points in the software pipeline. The design variable value steps also had to be carefully controlled so as to provide the MATLAB optimization function with the illusion that the problem landscape was smooth; in actuality, the problem landscape was discretized due to the rasterization of the simulated shim elements when modeling them in 3D space for use with the FT-based method. The bigger issue was a lack of confidence that the optimization was finding global minima, or reasonable approximations thereof. The arbitrary initial condition provided would determine the final solution. Randomizing this initial condition would make the optimization non-deterministic and thus non-reproducible, while providing an arbitrary one based on exploratory simulations and locations

expected to provide reasonable shimming efficacy by argument of geometry proved to result in synergistic shimming solutions of drastically different geometry and efficacy.

It was thus decided to use a deterministic, discretized comparison algorithm to evaluate the best combination of shim elements, as described earlier in the chapter. The main limiting factor was computation time, and to keep this within reasonable limits, we limited the number of discrete shim element locations in accordance with what was reasonable to implement using the shim frame hardware (see Specific Aim 2) and used the precalculated shim library computed using the more-efficient VOI-based FT method (see Chapter 3) as detailed previously.

2.4 Specific Aim 2: Develop Passive Shim Frame Hardware

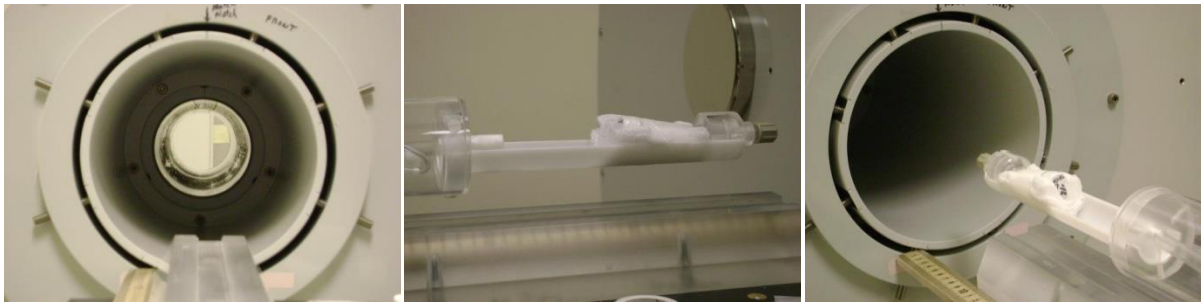

Figure 2.4. Photographs of the 7.0 T MR magnet used. (Left) The inner diameter of the magnet bore without body coil installed is approximately 11 cm. (Middle) The mouse animal bed. The shim frame is attached to this bed for mouse imaging. (Right) A size comparison between the magnet bore and the animal bed.

2.4.1 Shim Frame Main Tube Design

Experimental validation of the synergistic shimming method would require the design of a shim frame that could realize the placement of the passive shim elements within the bounds of the problem space presented by the magnet bore of our 7 T Bruker animal magnet and preexisting mouse bed. Photographs of the existing hardware are shown in Figure 2.4 above; the shim frame would have to be designed to fit around this bed and inside this bore.

The shim frame was designed as a multi-piece assembly that fits over the occupied mouse bed. The main structure is a hollow plastic tube that slips over the front part of the mouse bed. It is held at the correct height by two support pieces: one support ring snaps over the edge of the larger diameter section of the mouse bed (see left side of the center image of Figure 2.4) and holds the edge of the hollow tube within, while the other support ring slips over the nose cone assembly (right side of center image of Figure 2.4) and props up the hollow tube from the inside. The main tube has slots cut out to allow anesthesia and respiration monitor tubing to enter it; these are necessary for *in vivo* mouse experiments. It also has gradation marks to indicate distance in millimeters from the larger diameter section of the mouse bed; these are required for accurate positioning of shim elements in the *z* (axial) direction. The

CorelDraw laser cutter patterns for the shim frame support rings are shown in Figure 2.5 and a photograph of the main tube assembly is shown in Figure 2.6.

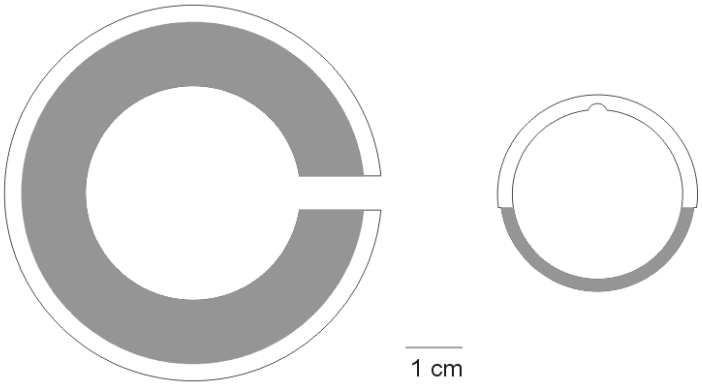

Figure 2.5. The CorelDraw laser cutter designs for the support rings. The gray fill represents areas that are to be etched rather than completely cut through.

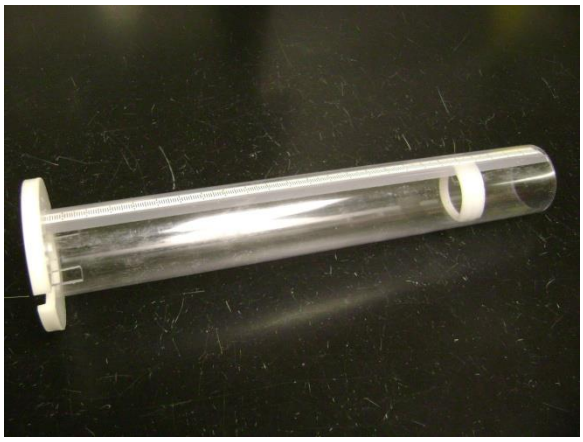

Figure 2.6. Photograph of the shim frame main tube assembly. The back support ring attaches to the mouse bed main tube and the front support ring rests upon the nose cone to keep the shim frame level with the mouse bed.

2.4.2 Passive Shim Element Design

A combination of ready availability of materials, non-toxicity, size, and efficacy in initial exploratory simulations guided the design of the passive shim elements. The shimming materials chosen to meet these criteria were graphite (χ = −116 ppm) and titanium (χ = 174 ppm), in the form of rods of ¼” (6.35 mm) diameter. (Rods and other materials sized in CGS units are often more widely available in the US than those with similar metric sizes.) Pieces of these needed to be produced in enough quantities that any given passive shim set could be implemented. To this end, rods of each material were acquired and machined to varying lengths from 5 mm to 25 mm, in steps of 5 mm, to match the possible shim element geometries used in the optimization algorithm. A few examples of shim elements are shown in Figure 2.7.

To avoid mismatch between the idealized cylindrical shim elements in simulation and the actual shim elements, several practical concerns had to be addressed. The initial cutting of the elements was performed with a band saw. In the case of the graphite, it was soft enough that the cut edges could be straightened and smoothened with only sandpaper. The titanium proved more difficult, as the initial cuts left sharp edges that had to be removed via a bench grinder. A lathe was also used to fix some of the rougher cut surfaces.

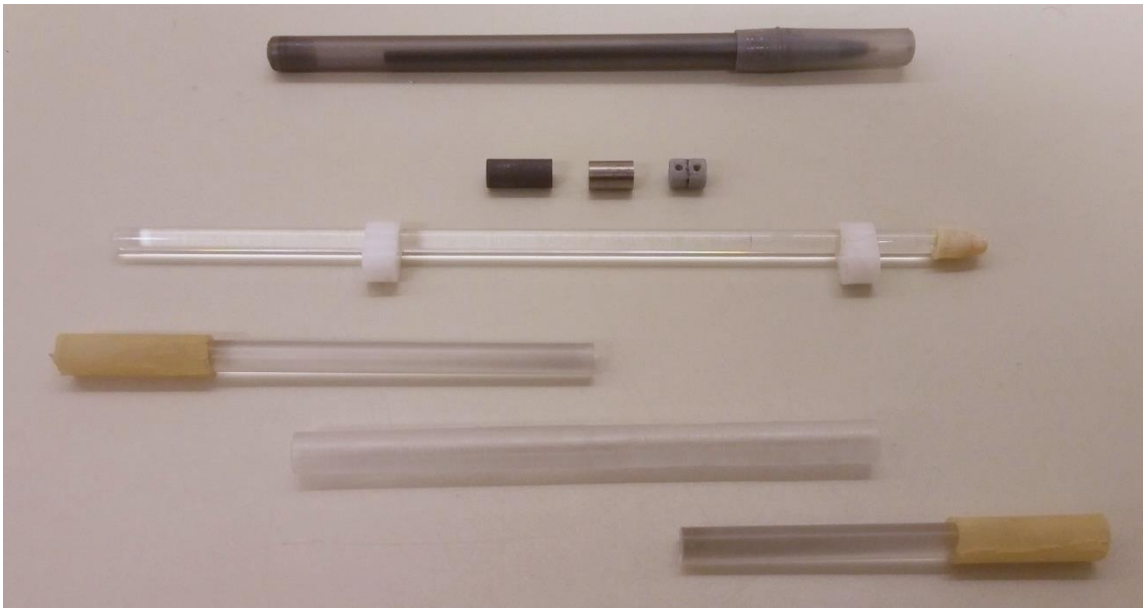

Figure 2.7. Photograph of various shim element placement and calibration components. From top to bottom: a pen (to show scale); a 15 mm graphite shim element, a 10 mm titanium shim element, the z-fiducial marker; an NMR tube fiducial cylinder; a latex rubber-capped plastic spacer rod, a hollow shim rod, and another spacer rod.

2.4.3 Shim Element Placement Design

The shim frame design is based on the idea that infinitely-long cylinders whose axes are parallel to the static B_0 field do not generate magnetic susceptibility-based static field inhomogeneities external to the cylinder (1). In practice, cylinders of finite length must be used to construct the frame components, but as long as they terminate far away from the volume of interest (VOI), their impact should be minimal. For this reason, it was decided to place the shim elements inside long, hollow plastic rods, which would then be filled with plastic spacers and suspended over the subject via shim rings. These shim rings were placed far to either side of the subject so as to avoid any significant impact on B_0 inhomogeneity within the VOI. A photograph of spacer rods and a hollow rod is shown in Figure 2.7 and a photograph of the shim rod assembly mounted to the frame is shown in Figure 2.8.

Figure 2.8. Photograph of the shim frame with a mounted shim rod assembly and fiducial cylinder. The spacer rods, hollow rod, and titanium shim element composing the shim rod assembly are the same as the ones shown in Figure 2.7.

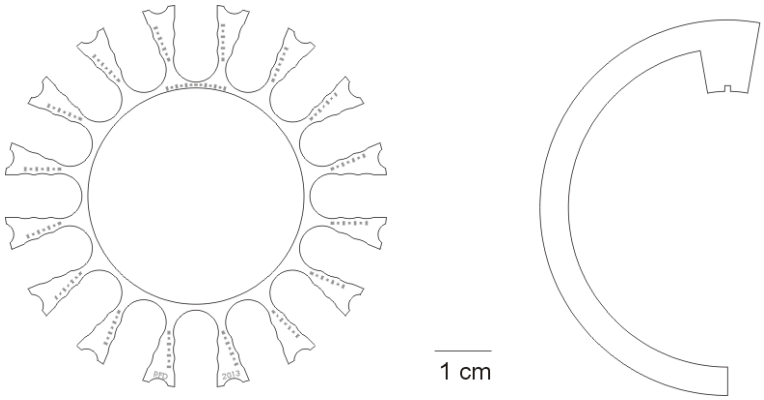

Figure 2.9. The CorelDraw laser cutter designs for the shim rings (left) and positioning tool (right).

The shim rings (white starburst shapes in Figure 2.8) smoothly slide along the main tube of the shim frame yet fit tightly around the tube so that they remain in place. This was accomplished by slowly scraping away at the plastic of the inner surface of the ring until the exact diameter needed to achieve this effect was reached. Each shim ring is a circular, laser-cut piece of plastic; the laser cutter pattern is shown in Figure 2.9. The outer diameter of the shim ring was 67.4 mm such that the ring, once mounted on the shim frame, would not bump into the RF coil when pushed into the magnet. In the space between the outer and inner diameters, several holes designed for mounting shim rods were cut. These holes were spaced 22.5° apart

and featured a notched design that allowed the rods to “snap” into place at radial distances of 24 mm, 27 mm, and 30 mm between the center of the rod and the center of the frame. Each hole also has gradation marks in the radial direction spaced 1 mm apart that could allow for finer adjustment of the rod position in the radial direction. The design diameter of the holes was 7.9375 mm, equivalent to the diameter of a ¼” (6.35 mm) diameter shim element contained inside a 1/32” (0.79375 mm) wall thickness hollow rod. In practice, the holes were designed slightly smaller, at 7.91 mm, to account for the laser cutter’s cut width. The shim rings also have etched markings in 1° intervals underneath the first hole for precise rotation of the shim ring with respect to the shim frame. The shim rings were placed 50 mm away from the center of the volume of interest to minimize their impact on the B_0 field.

To create the hollow plastic shim rods (bottom-center of Figure 2.7), hollow plastic tubes with ¼” (6.35 mm) inner diameter were acquired, machined down to 7.9375 mm outer diameter, and cut to 110 mm lengths. To create the plastic spacer rods (bottom-left and bottom-right of Figure 2.7), solid ¼” (6.35 mm) diameter plastic rods were cut to varying lengths (45 mm, 75 mm, and 105 mm) and the ends encased in 1/32” (0.79375 mm) wall thickness latex rubber tubing. This tubing was chosen due to its good cushioning and dampening properties, ensuring that a plastic rod would not easily move from its position once placed within a shim ring, e.g., due to vibrations caused by sliding the mouse bed in and out of the magnet bore or gradient switching during scanning.

The bare portions of the spacer rods fit inside the hollow rods to sandwich the passive shim elements on either side, and the hollow rods and the tubing-encased portions of the spacer rods slot into the shim rings, which hold them snugly in place, as shown in Figure 2.8. The outer edges of the shim rings were designed to be open, so insertion and removal of the rods could be done in-place and so the rings had flexibility to securely grip the hollow rods. In this way, only long, cylindrical objects are nearby the subject. Effectively, each shim rod assembly consists of an “invisible” long plastic rod superimposed with one or more passive shim

elements and plastic holes of the same geometries and positions (and thus same correction field shapes) as the passive shim elements. Therefore, this design allows for precision passive shim element placement without significant impact on the B_0 homogeneity within the VOI.

In order to accurately position shim elements in the z (axial) direction, a positioning tool was cut from ¼" (6.35 mm) thick acetal plastic. The design for this tool is shown in Figure 2.9 and a photograph is shown in Figure 2.10. The tool's head can be placed against the shim frame main tube's gradation marks and the curve against the shim rods to visually determine the position of a passive shim element with respect to the gradation marks. This sort of measurement is subject to parallax error; to avoid this, the back edge of the tool is marked in black marker, and prior to reading the measurement of position, the user's viewing angle is adjusted until the front and back edges of the tool are just overlapping.

Figure 2.10. Photograph of the positioning tool.

2.4.4 Calibration

In order to verify that the simulation space maps to the laboratory space, it was necessary to develop a calibration process. In this process, fiducial markers consisting of volumes of MR signal source of known geometry and position with respect to the shim frame are placed into the magnet along with the subject, and the geometry and position of the fiducial markers within the measured MR image are quantified.

In order to measure offset in the three translational (x/y/z) and rotational (pitch/roll/yaw) directions, it was decided to use two long cylinders and one extremely thin cylinder of signal as the fiducial markers. The long cylinders were created by filling glass NMR tubes of 4 mm inner diameter with water, capping them with rubber caps, and then inserting the tubes into plastic inserts cut from a sheet of ¼" (6.35 mm) acetal plastic using a laser cutter. The NMR tubes could then be inserted into the shim frame via the inserts. The design for these inserts is shown in Figure 2.11, and the fiducial cylinder assembly as a whole is shown in Figure 2.7. Typically, these were placed at the -45° and 135° positions in the shim frame as the diagonal positions are best included in the cubical VOI of the MR scan.

Figure 2.11. The finished CorelDraw laser cutter pattern for the plastic insert for the fiducial cylinders.

The thin cylinder, or z-fiducial marker, was created by designing a small cylinder in the SolidWorks computer-aided design software (Dassault Systèmes, Vélizy-Villacoublay, France) and printing it using a 3D printer (Ultimaker, Geldermalsen, Netherlands). This cylinder was of ¼" outer diameter and contained a thin, 0.7 mm hollow disc of 4 mm diameter connected by tunnels to the side of the cylinder. Using a 26-gauge syringe needle, water could be injected

through the tunnels and into the disc area, which would then appear in the MR image. The outside surface of the cylinder was slightly indented at the location of the internal disc and marked with black marker so as to make visual identification of the location of the disc of water easy during placement. The SolidWorks schematic for the z-fiducial marker is shown in Figure 2.12, and a photograph in Figure 2.7. Typically, this disc was placed at a known location along the shim frame (e.g., at the 135 mark) and at the 45° position.

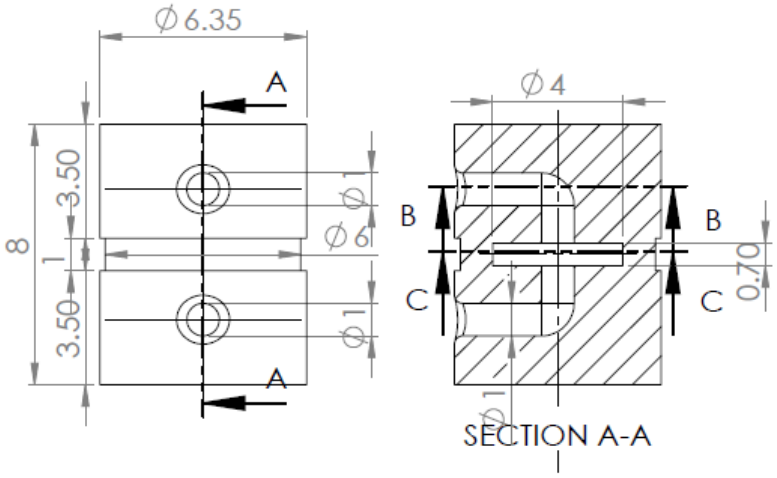

Figure 2.12. Schematic of the z-fiducial marker. All units are in millimeters (mm).

Once all fiducial markers are mounted in the frame at the specified locations, the initial B_0 field map is acquired. This scan includes magnitude image data, which contains the signal regions from the fiducial markers. It is this data that is examined by the calibration algorithm. First, the region inside the shim frame, including the subject, is removed. Then, a 2-standard-deviation-above threshold is used to identify the signal regions in the area comprising the shim frame. The algorithm then simulates long cylinders of signal of the same dimensions as the designed cylinders and checks predetermined axial slices for the presence of these cylinders at each slot angle in the shim frame. It determines a cylinder to be found if there is sufficient cross-sectional area overlap between a simulated and measured cylinder. It was empirically found that

a value of 20% or more overlap worked well to identify the existence of a cylinder without spurious false positives.

Once cylinders are found, it then simulates cylinders with different θ offsets, corresponding to the shim frame having a rotational offset in the roll direction with respect to the magnet imaging axes. It also performs a directed search in the transverse (x and y) directions. Whichever combination of offset values in θ, x, and y that produces the greatest cross-sectional area overlap between the simulated and measured cylinders is accepted to be the correct set of calibration values. If the roll direction (θ) offset is too large, greater than about 2° from center, the user should rotate the frame about the animal bed to correct for this and recalibrate. The regions encompassing the simulated cylinders are then removed from the magnitude image as well, leaving, in theory, only the signal from the thin disc cylinder. This is then located using a similar simulation-based search and thresholding, and the axial slice in which the disc is present noted.

Finally, orthogonal views of the long cylinders found are presented to the user to ensure that there is no significant rotation in the pitch and yaw directions, as this would be difficult to correct for in simulation and would further cause severe subject alignment issues. If there is significant rotation, the user must adjust the bed and frame height with respect to the magnet bore and RF coil and recalibrate to ensure that there is no such rotation. An axial filmstrip view of the thin disc cylinder is presented to ensure that the z-fiducial marker was located in the correct axial slice, as shown in Figure 2.13. In case the algorithm is unsure as to the location of the z-fiducial, multiple candidate slices are presented for the user to choose. In this way, it is ensured that there is no significant rotation in the pitch, yaw, and roll (θ) directions, that any transverse translation (x and y) is accounted for, and that the simulation space axial axis (z) maps to the laboratory space axis via a thin disc of signal that has been visually placed at a location along the shim frame and located in the acquired image.

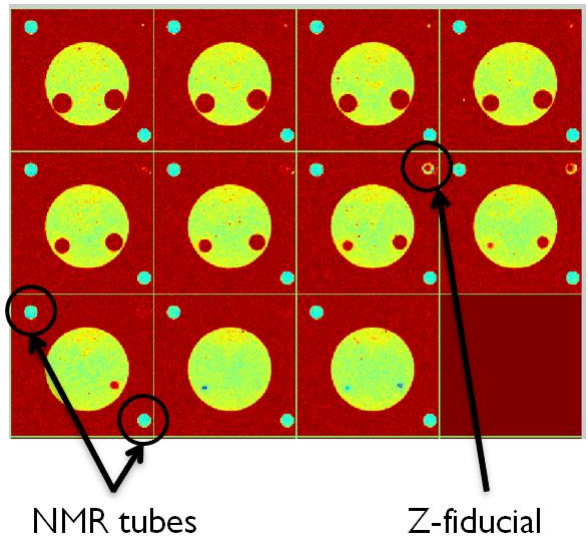

Figure 2.13. Example of axial filmstrip presented to user following calibration. Sample in center is an agar air bubble phantom (shown in Figure 2.16).

2.4.5 Shim Frame Development and Challenges

Previously, the frame implemented placement of passive shim elements by encasing the elements in rubber tubing and placing the elements into closed, rigid plastic shim rings. The shim rings could then slide back and forth along the frame's main tube to adjust the shim elements' positions in the z direction, as shown in Figure 2.14 below. It was initially believed that these rings would not have a significant effect on the B_0 field. However, it was found that this design created its own susceptibility-induced inhomogeneity due to the rings' short length in the axial (z) direction and large cross-sectional area. Once the geometry of the plastic rings was included in the simulated B_0 field difference maps with and without the rings, the simulation matched the experimentally acquired difference maps. However, this was an undesirable condition, as it imposed a specific, unitary correction field shape to be superimposed with the passive shim element's variable correction field, destroying the flexibility of the shimming system. For this reason, the shim frame hardware was redesigned to its current form, placing

shim rings far away from the VOI and using long, axially-oriented cylindrical shapes to position the shim elements.

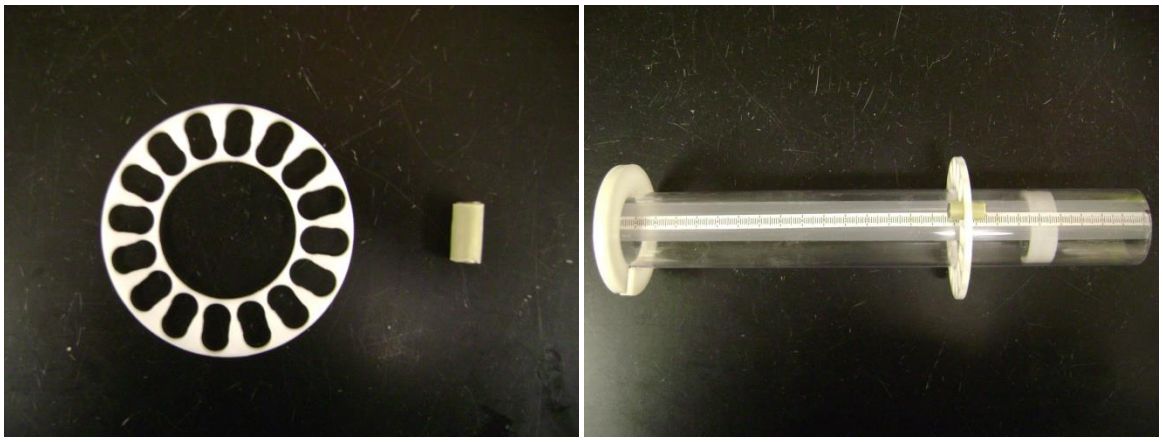

Figure 2.14. The previous version of the shim frame assembly. (Left) A shim ring and shim element (latex rubber-wrapped titanium). (Right) The main tube with a shim ring and shim element mounted on it. This shim ring would slide back and forth to position the shim element in the z direction.

2.5 Validation

2.5.1 Shim Element Placement Validation

In order to confirm that the shim frame hardware could indeed position shim elements as dictated by the optimization software, a shim element placement validation experiment was performed. An imaging phantom composed of a 50 mL graduated cylinder tube filled with agar was placed in the mouse animal bed, and the shim frame was mounted on the mouse bed as well. The z-fiducial marker was placed at a specific distance mark (125 mm) along the shim frame main tube. The phantom, frame, and bed were inserted into the magnet and positioned such that the isocenter of the magnet lay roughly in the center of the agar phantom. A tripilot scan was performed to ensure reasonable positioning. A B_0 field inhomogeneity map was then acquired using the Bruker FieldMap sequence.

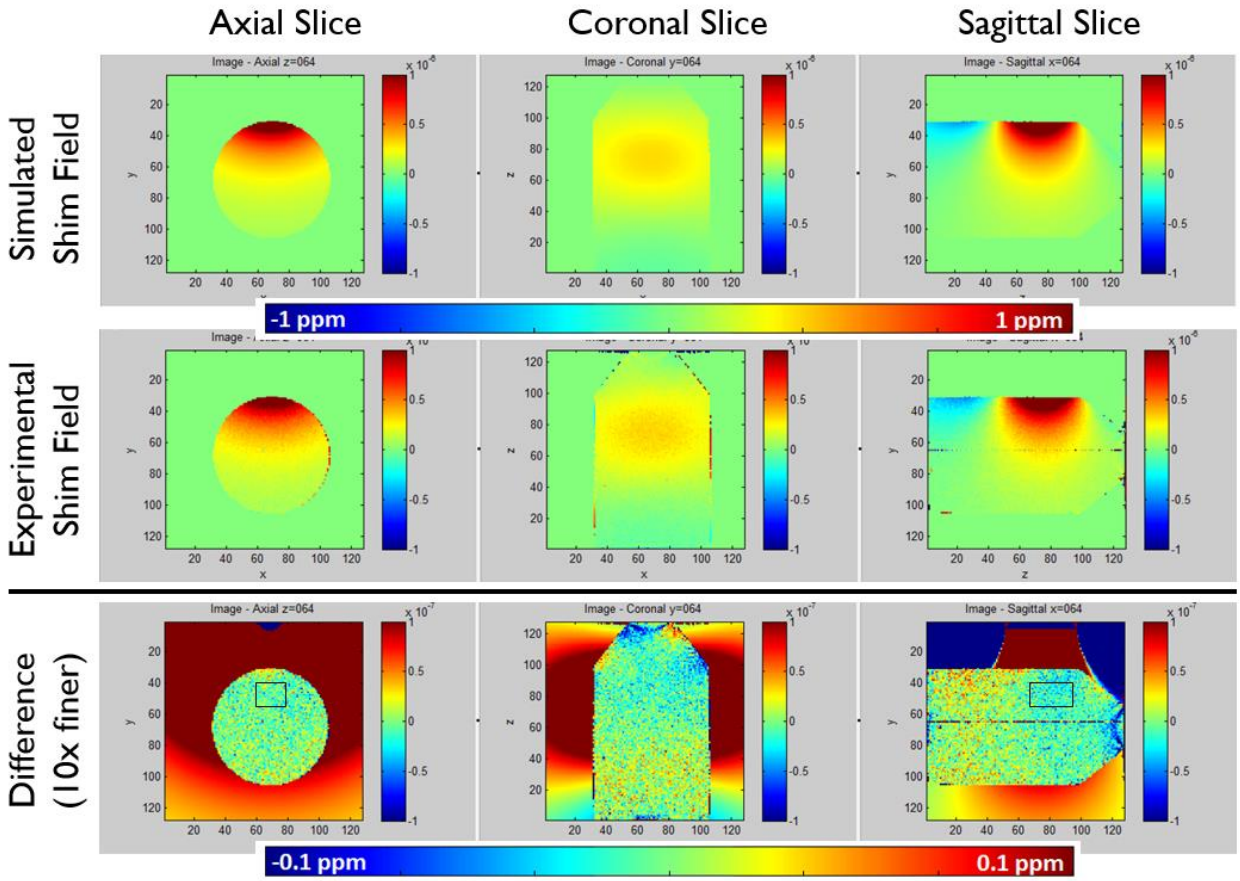

Figure 2.15. Comparison of the B_0 perturbation fields of a simulated graphite shim element and an actual graphite shim element. The axial, coronal, and sagittal slices through the center of the phantom are shown. The VOI used for quantification is shown in black outline. The simulation and experiment are largely in agreement. The color scale has bounds of ±1.0 ppm (±300 Hz) in the first two rows and ±0.10 ppm (±30 Hz) in the last row.

In simulation, a single 16 mm-long graphite shim element was placed above the phantom at the equivalent of the 135 mm mark and its resulting B_0 perturbation field computed. The animal bed was then retracted from the magnet, a 16 mm-long graphite shim element was mounted on the frame at the 135 mm mark, and the bed was reinserted. A second B_0 field inhomogeneity map was then acquired. The first map was subtracted from this second map to obtain the experimentally measured B_0 perturbation field of the shim element alone. These two B_0 perturbation fields of the same graphite shim element, one computed via simulation and one

obtained via experiment, were then compared, as shown in Figure 2.15 above. The simulation and experiment agree quite well, with a mean difference of 0.0179 ppm and a standard deviation of the difference of 0.0192 ppm within a rectangular volume of interest (VOI) near the shim element (shown in black outline).

This demonstrated two things: that the simulation algorithm can indeed simulate the B_0 perturbation effects of shim elements with reasonable accuracy, and that the shim frame can be used to mount shim elements in accordance with a specified passive shim configuration, e.g., an output solution from the synergistic shimming optimization algorithm.

Figure 2.16. The air bubble phantom. The two air bubbles (hollow green plastic spheres) can be seen within (white arrows). A pen is also shown for size comparison.

2.5.2 Localized Synergistic Shimming Validation

Now that this was established, we decided to validate the synergistic shimming system as a whole. For the experimental validation, an air bubble phantom approximating the mouse head was created using a 50 mL graduated cylinder tube. The tube was halfway filled with a mixture of warm 2% agar gel and sodium azide (to prevent bacterial growth). When the agar was partially set, two hollow HDPE plastic spheres (design outer diameter = ¼”, measured inner diameter = 4 mm) were added to roughly simulate the posterior maxillary sinuses of the mouse,

and more agar was added to fill the tube. The agar was allowed to set, and the mouth of the tube was covered with parafilm. The phantom is shown in Figure 2.16 above.

A thin rectangular VOI representing temporal lobe brain regions nearby the simulated ear canals was selected above the dual air bubbles as the region to be synergistically shimmed. A B_0 map of the phantom was acquired. The VOI was shimmed using linear active shimming alone as a baseline for comparison, and a B_0 map of this acquired. The original B_0 map was input into the optimization algorithm, and a shim solution was output involving a 15 mm graphite shim element and a 5 mm titanium shim element, as shown in Figure 2.17 below. The mouse bed and phantom were slid out of the magnet, the two shim elements were mounted onto the shim frame, and a second B_0 map was acquired. We then compared the field maps and the ΔB_0 variance within the VOI for linear active shim case, simulated synergistic shim case, and the experimentally acquired synergistic shim case. The images qualitatively demonstrating the improved shim homogeneity within the VOI are shown in Figure 2.18 and the quantitative results are shown in Table 2.2. We observed a 46% reduction in the variance within the VOI. This demonstrates that the system as a whole works to improve ΔB_0 homogeneity within the VOI.

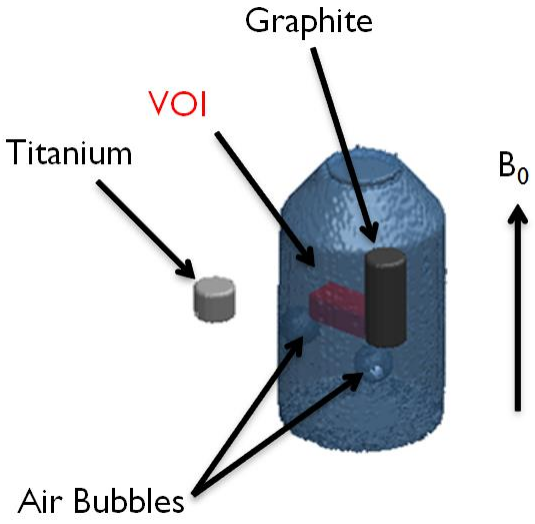

Figure 2.17. A 3D rendering of the agar air bubble phantom, the VOI selected, and the shim configuration tested.

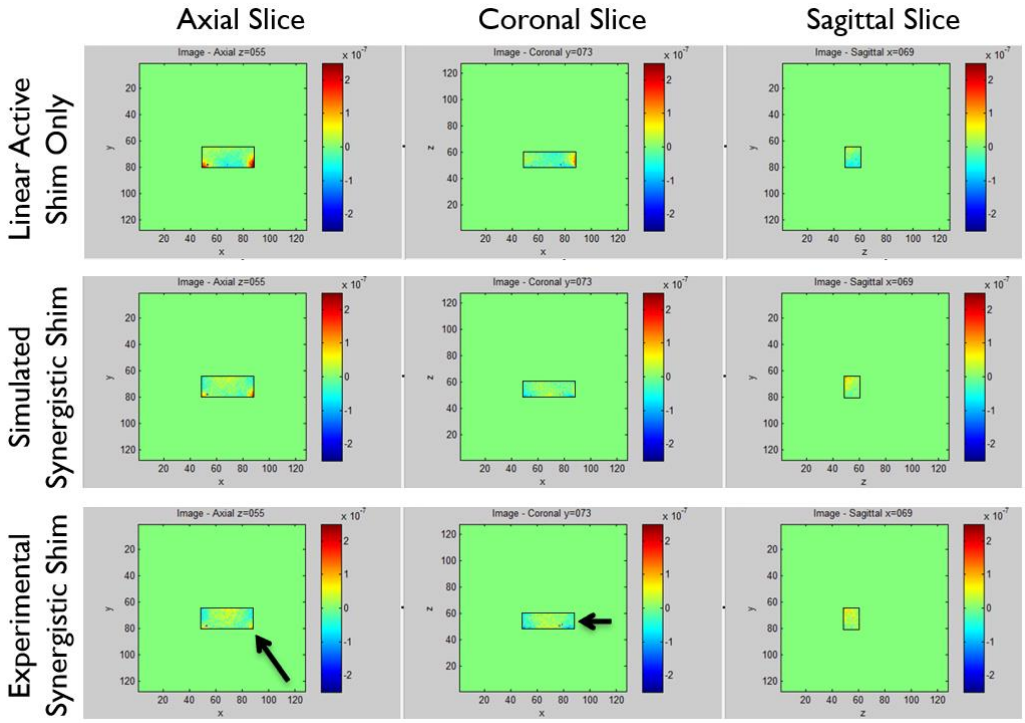

Figure 2.18. Visual comparison of ΔB_0 within the VOI for the agar air bubble phantom before and after synergistic shimming. Note the reduction in strong gradients in the corners, nearest the air bubbles.

Table 2.2. Variance within the VOI for the agar air bubble phantom before and after synergistic shimming.

Case	Variance	Percent Change
Linear Active Shim Only	22.6756	–
Simulated Synergistic Shim	12.3739	−45.6%
Experimental Synergistic Shim	12.2461	−46.0%

2.6 Discussion

We designed a synergistic shim system to improve ΔB_0 homogeneity within a targeted VOI. This system is designed such that the frame hardware does not itself alter the shimming problem within the VOI and is constructible out of widely available, inexpensive materials. We

additionally validated both placement of shim elements using the system and the system as a whole within a VOI inside an air bubble phantom representing a mouse head. By experimentally demonstrating an improved shim that agrees with the simulation, we showed that the system as a whole works as expected, suggesting that it can indeed be potentially used to shim *in vivo* subjects, such as mice.

The current software optimization algorithm is essentially a brute-force approach that examines all possible combinations of shim elements according to the design rules. Currently, the algorithm is designed to add passive shim elements to the total shim configuration one at a time. This is adjustable; the possibility to add two, or even three, shims at a time is already implemented and was explored. Doing so should theoretically improve the shim results by exploring more of the search space of possible shim configurations, e.g., by finding solutions wherein a combination of two shim elements is very efficacious despite each individual element worsening the shim result if taken alone. However, doing so also exponentially increases the number of combinations to be checked, and thus the run time. The current algorithm, adding one shim element at a time, takes about 80 seconds to finish running on our workstation (a dual hex-core 2.66 GHz Intel (Intel Corporation, Santa Clara, CA) Xeon X5650 workstation with 36 GB RAM and running 64-bit Windows). Checking two shim elements at a time using a far lesser number of candidate shim elements took about 30 minutes, while three at a time would take days, and the run was aborted. In the exploratory test cases considered, adding shim elements two at a time did not appear to yield significantly better shim configurations, so the current approach was adopted to minimize time taken, which would be important for *in vivo* studies. One avenue of improvement would be to once again explore the use of intelligent metaheuristic approaches—perhaps, this time, ones specialized for discretized problems—to explore more of the problem search space than the current approach without lengthening the run time to levels unacceptable for *in vivo* applications.

The current shim frame hardware is a simple system in which the shim elements must be manually mounted and adjusted in accordance with the optimization software. The simplicity of the design allows for a reasonably high degree of flexibility in shim element positioning within the tight confines of the magnet bore. However, it also necessitates that the subject bed be slid out of the magnet to implement changes to the passive shim element configuration and then slid back in to precisely the same location. For magnets with a manual subject bed, such as ours, rather than an automated bed, this is not ideal, as it can be difficult to return the subject to exactly the same position. From our experiments, an error in returning the subject to the original position of about ±0.5 mm was observed. For such systems, it might be ideal to have a different shim frame design that is adjustable while it remains inside the magnet, perhaps using long adjustment rods that can be reached from outside the bore.

The frame geometry and range of sizes and positions of the candidate shim elements was designed taking into account the available space within the magnet bore, the existing animal bed hardware, and the estimated shim field requirements based on the air bubble phantom. The geometry may need to be redesigned for other applications with differing bore sizes and subject beds. It may be preferable to design a frame that fits closer to the subject, or fits outside the RF coil, depending upon the application. In our case, exploratory simulations suggested that a frame as close as possible to the subject would be most appropriate for application to mouse brain shimming.

3 VOI-based Fourier Transform Method for Calculation of Static Magnetic Field Maps from Susceptibility Distributions

In this section, the impetus for developing the VOI-based Fourier Transform method will be discussed. Development of the method was initially motivated by a desire for increased speed during the computation of passive shim element perturbation fields. However, it was found to also have potential applications in high-resolution anatomic field computations that might require large amounts of computer memory (RAM). The merits of the method were therefore demonstrated using both such computations as example applications.

3.1 Introduction

The increasingly common use of high field strength MR magnets exacerbates magnetic susceptibility-induced static magnetic field (B_0) inhomogeneity artifacts (4). For *in vivo* studies, subject-specific B_0 inhomogeneity (ΔB) field maps are often used to correct these artifacts in a variety of ways, such as via retrospective post-processing (29), adjustment of the magnet's active shim sets (30), custom multicoil active shims (31), or adaptive passive shimming (18,32). In certain applications, it is desirable to numerically calculate the ΔB field map based on subject-specific geometry. For example, in breast shimming optimization, the presence of multiple chemical species (i.e., fat, soft tissue, and silicone) causes undesirable chemical shift and phase wrapping artifacts in the acquired field map. These problems can be avoided by instead calculating the field map from segmented anatomical images (33). In this and other cases in which experimental acquisition of the field map is difficult or confounded by imaging artifacts, the calculated field map can be used instead for artifact correction (34). Furthermore, in optimization of a passive shimming process, to measure the B_0 field perturbation of every possible shim configuration is impossible. It would be ideal to be able to numerically calculate the B_0 field perturbation of such passive shimming elements rapidly (18).

To address this issue, a method for calculating the ΔB field map resulting from an arbitrary magnetic susceptibility distribution via Fourier Transform convolution of the susceptibility distribution with a dipole kernel was previously developed (12,20,35,36). This method involves a forward and inverse Fourier Transform of the entire matrix representing the susceptibility distribution of the problem region. This operation can have high computational memory and time requirements for large matrices, such as for high-resolution whole-body human models, necessitating the use of dedicated, expensive workstations rather than MRI consoles. Recently, a more efficient method for calculating the resultant ΔB field maps in individual slices of a subject was developed (33). However, this method is still time-inefficient when calculating the ΔB maps of multiple slices, rendering its use in an "online" B_0 artifact correction method that is performed while the human subject is within the magnet infeasible.

Here, we present a volume of interest (VOI)-based approach that calculates the ΔB field in a small portion of the full high-resolution computer model without introducing truncation error due to reduction of the problem region as in the conventional method (37). Our method has lower memory requirements than the conventional method and similar or lower time requirements than the conventional or slice-based methods when used on "sparse" matrices wherein the susceptibility sources and regions of interest comprise a relatively small portion of the total susceptibility matrix. We demonstrate that the VOI-based method is effective for passive shim applications and subject-specific localized ΔB field map calculation applications.

3.2 Theory

The conventional Fourier Transform-based static magnetic field calculation method uses a convolution of a three-dimensional dipole Green's function kernel with the susceptibility distribution to calculate the resultant B_0 field inhomogeneity map, ΔB (12). In this method, the Green's function is computed in the k-space domain:

$$\Delta B(\vec{r}) = B_0 \cdot FT^{-1}\left\{G(\vec{k}) \cdot FT\{\chi(\vec{r})\}\right\}, \text{ where } G(\vec{k}) = \frac{1}{3} - \frac{k_z^2}{k_x^2+k_y^2+k_z^2} \qquad [3.1]$$

The method by Cheng et al. (20) instead computes the Green's function in the image domain and then applies the 3D Fourier Transform, resulting in proper discretization of the Green's function in k-space:

$$G(\vec{k}) = FT\left\{\frac{1}{4\pi} \cdot \frac{2z^2-x^2-y^2}{(x^2+y^2+z^2)^{\frac{5}{2}}}\right\} \quad [3.2]$$

$$G(\vec{r}) = \frac{1}{4\pi} \cdot \frac{2z^2-x^2-y^2}{(x^2+y^2+z^2)^{\frac{5}{2}}} \quad [3.3]$$

This can be taken a step further by noting (33,35) that this equation can be used to express the effect of a single source susceptibility voxel at $\vec{r}'$ on the ΔB field in a single target voxel at $\vec{r}$, solely in the image domain, as shown in Eqs. 3.4 and 3.5:

$$\Delta B(\vec{r},\vec{r}') = B_0 \cdot G(\vec{r}-\vec{r}') \cdot \chi(\vec{r}') \quad [3.4]$$

$$\Delta B(\vec{r},\vec{r}') = B_0 \cdot \frac{1}{4\pi} \cdot \frac{2(z-z')^2-(x-x')^2-(y-y')^2}{((x-x')^2+(y-y')^2+(z-z')^2)^{\frac{5}{2}}} \cdot \chi(\vec{r}') \quad [3.5]$$

By integrating $\vec{r}'$ over the region of varying susceptibility, v', this approach can be used to find the total susceptibility-induced B_0 inhomogeneity field:

$$\Delta B(\vec{r}) = \int_{v'} B_0 \cdot G(\vec{r}-\vec{r}') \cdot \chi(\vec{r}')\, d\vec{r}' \quad [3.6]$$

A key point to note is that v' and the VOI within which to evaluate $\Delta B(\vec{r})$ need not be coincident and can be at a distance from each other (33). In the conventional method, the effective volume of integration v', the "source", and the VOI, the "target", both consist of the entire problem region. However, by narrowing v' such that it contains only the susceptibility source and limiting the evaluation of $\Delta B(\vec{r})$ to only the VOI, one can significantly reduce the amount of computation required to determine the effect of the susceptibility source on the ΔB field in the target VOI.

In order to apply the convolution theorem to Eq. 3.6 so that the 3D Fast Fourier Transform (3DFFT) may be utilized for improved computation speed, the quantities being numerically convolved must have the same matrix size and must have consistent coordinate axes, with the volume of integration centered about the origin. In the conventional method,

these criteria are met by default as the matrices being convolved span the entire problem region:

$$\Delta B(\vec{r}) = B_0 \cdot FT^{-1}\{FT\{G(\vec{r})\} \cdot FT\{\chi(\vec{r}')\}\} \quad [3.7]$$

However, when performing a targeted, VOI-based calculation on only portions of the full problem region, a change of variables is required to ensure that both convolved matrices have consistent coordinate axes.

Let $\vec{p}$ be a vector from the origin to the center of the target VOI and $\vec{p}'$ be a vector from the origin to the center of the source subregion of χ, as illustrated in Figure 3.1a. We then define the shifted susceptibility distribution, $\chi_s(\vec{r}') = \chi(\vec{r}' + \vec{p}')$, and the shifted resultant Δ*B* distribution, $\Delta B_s(\vec{r}) = \Delta B(\vec{r} + \vec{p})$. These shifted distributions are translations of the susceptibility and Δ*B* distribution subregions to the origin of the coordinate space. We similarly define shifted variables $\vec{r}_s = \vec{r} - \vec{p}$ and $\vec{r}_s{}' = \vec{r}' - \vec{p}'$. These represent the target and source vectors translated into the shifted coordinate space. Finally, we define the shifted Green's function, $G_s(\vec{r}) = G(\vec{r} + \vec{p} - \vec{p}')$. By substituting these shifted quantities into Eq. 3.6, we shift the source susceptibility subregion and volume of integration such that they are centered about the origin:

$$\Delta B_s(\vec{r}_s) = \int_{v_s'} B_0 \cdot G_s(\vec{r}_s - \vec{r}_s') \cdot \chi_s(\vec{r}_s{}')\, d\vec{r}_s{}' \quad [3.8]$$

We can then apply the convolution theorem as normal:

$$\Delta B_s(\vec{r}_s) = B_0 \cdot FT^{-1}\{FT\{G_s(\vec{r}_s)\} \cdot FT\{\chi_s(\vec{r}_s{}')\}\} \quad [3.9]$$

and then back-substitute to revert to unshifted space to obtain the expression for the new VOI-based calculation method:

$$\Delta B(\vec{r}) = B_0 \cdot FT^{-1}\{FT\{G(\vec{r} - \vec{p}')\} \cdot FT\{\chi(\vec{r}')\}\} \quad [3.10]$$

Figure 3.1b further illustrates the concept of the VOI-based Fourier Transform B_0 calculation method. As per Eq. 3.10, the portion of the Green's function originating from the susceptibility source region and overlapping the VOI is convolved with the susceptibility source to obtain the Δ*B* distribution in the VOI. The numerical calculation of $FT\{G(\vec{r} - \vec{p}')\}$ is performed

by translating $\vec{r}$ by $\vec{p}'$ prior to computing $G(\vec{r})$ using Eq. 3.3 and then performing the 3D Fourier Transform with respect to $\vec{r}$.

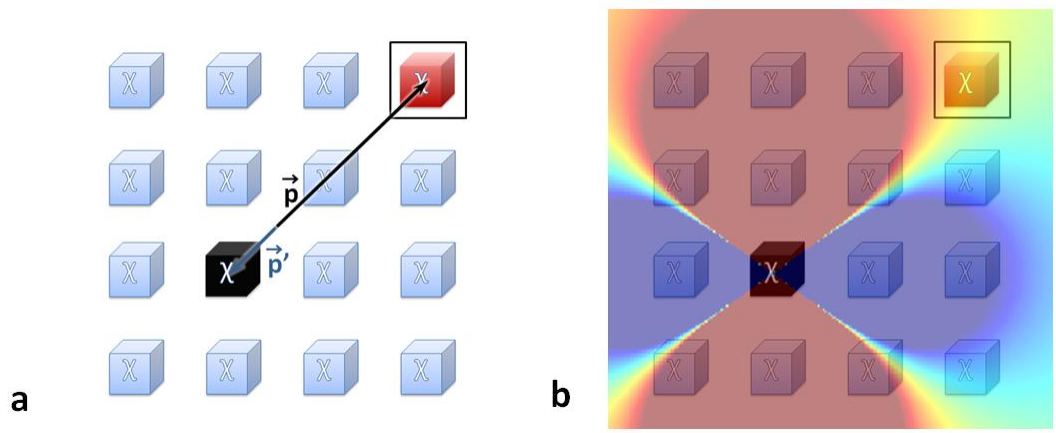

Figure 3.1. An illustration of the VOI-based ΔB field calculation method. To calculate the effects of a source susceptibility region (black) centered at $\vec{p}'$ on the ΔB field in a target VOI region (red) centered at $\vec{p}$, the portion of the image domain Green's function, absent in (a), overlaid in (b), originating from the source region and overlapping the target region (black outline) is convolved with the source susceptibility region (black).

In the implementation of the above algorithm, multiple source and target (VOI) regions can be defined, and the effects of multiple source regions on the Δ*B* field in a given target region are summed in linear superposition. If there are *S* source regions and *T* target regions defined, the number of 3DFFT computations required is as follows. The forwards 3DFFT of the susceptibility matrix $\chi(\vec{r}')$ must be performed once for each source region. The evaluation of the Green's function matrix $G(\vec{r}-\vec{p}')$ and its forwards 3DFFT, as well as the inverse 3DFFT of the product $FT\{G(\vec{r}-\vec{p}')\}\cdot FT\{\chi(\vec{r}')\}$, must each performed once per combination of source and target region. The total number of 3DFFTs that are computed is thus *S* + 2*ST*. Each source region is also zero-padded to double its size along each dimension, and the corresponding Green's function subregions oversampled by a factor of 2 in each dimension as well, to avoid

Fourier ghosting artifacts (35). By subdividing the conventional Fourier Transform calculation such that empty source regions and target regions that are not of interest are excluded, reductions in computation memory can be achieved.

3.3 Methods

3.3.1 Validation in a Phantom Simulation

The algorithm was validated via a simple phantom with a known analytical solution. For a sphere of homogeneous material with susceptibility χ_i and radius R placed within a background region of susceptibility χ_e, the ΔB field is given by (12,20):

$$\Delta B(\vec{r}) = \begin{cases} \frac{1}{3}(\chi_i - \chi_e)B_0 R^3 \frac{2z^2 - x^2 - y^2}{(x^2+y^2+z^2)^{\frac{5}{2}}} + \frac{1}{3}\chi_e B_0, \ r > R \\ \frac{1}{3}\chi_e B_0, \ r < R \end{cases} \quad [3.11]$$

The phantom consisted of a water sphere (χ = −9.0 ppm) with a radius of 12 voxels placed in a background region of air (χ = 0.4 ppm) with 128×128×128 matrix size. For testing purposes, 8 non-overlapping box regions, together encompassing the sphere, were chosen as su;sceptibility source regions for the VOI-based method, as shown in Figure 3.2a. Two target VOI regions were chosen, as illustrated in Figure 3.2d: one including a portion of the sphere and the surrounding region, and the other near the edge of the simulation region. Each individual susceptibility source region and target VOI region was of the arbitrary size 24×40×30 voxels. The resultant ΔB field in these target regions was calculated using the proposed VOI-based method and compared to the ΔB field calculated using the existing whole-volume Fourier Transform-based calculation method and using the above analytical solution. All simulation experiments were performed in MATLAB (The MathWorks, Inc., Natick, MA).

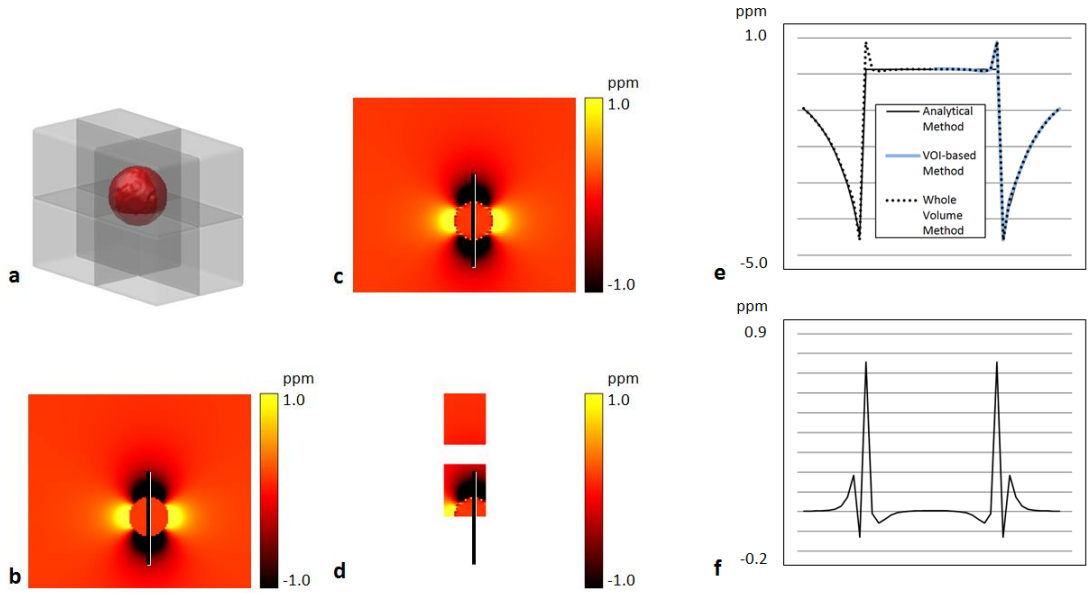

Figure 3.2. VOI-based Δ*B* calculation method phantom simulation results: A 3D model of the water sphere (red; *R* = 12 vx) and the 8 source susceptibility regions chosen to encompass it (a). The calculated Δ*B* field using the analytical method (b), conventional Fourier Transform method (c), and VOI-based Fourier Transform method (d). (The VOI-based method calculates the field map only in the target VOI regions.) A line plot through the center of the sphere (profile line shown in b, c, and d) in the axial direction demonstrates that the VOI-based method produces valid results identical to the conventional whole-volume method (e). A line plot of the difference in calculated Δ*B* field between the VOI-based method and analytical method along the same profile line demonstrates the error in the VOI-based method resulting from discrete quantization effects, which matches that shown in the conventional method (f).

3.3.2 Application to a Human Body Model Simulation

The efficiency of the algorithm was evaluated by calculating the B_0 field distribution within the brain and heart of a human body model using both the conventional whole-volume calculation method and the VOI-based method. The computation time and memory required by these two methods were compared. In addition, the efficacy of reducing the size of the problem region by truncating some of the source susceptibility data as an alternative way to reduce computation time and memory using the conventional method was also evaluated.

The model used was Duke from the Virtual Family Project, at 2 mm isotropic voxel resolution with 270×142×902 matrix size. The matrix was cropped to remove empty voxels, and the various anatomical structures within the model were assigned magnetic susceptibility values as shown in Table 3.1. A 72×92×72 voxel region that encompassed the whole brain was chosen as the volume of interest (VOI) for the first set of calculation experiments, and a 76×58×60 voxel region encompassing the heart chosen as the VOI for the second set.

The ΔB field map in the brain VOI and the heart VOI resulting from the susceptibility distribution of the whole human body was calculated using the conventional whole-volume Fourier Transform calculation method. This was compared to the field maps in the VOIs computed using truncated human body models. The models evaluated for the brain VOI are shown in Figure 3.3a: the full model and the partial models with the portion below the waist removed, below the middle of the torso removed, and with the head only. The models evaluated for the heart VOI are shown in Figure 3.3b: the full model and the partial models with the portion below the thighs removed, below the waist removed, and with only the torso region surrounding the heart. Error maps were created for each of the cases by computing the voxel-wise difference between each truncated-model calculated field map and the gold standard whole-model calculated field map. The mean percent error in calculated ΔB value for all voxels within the VOI was also computed for each case. The proposed VOI-based ΔB calculation method

was then used to calculate the field map in the VOI resulting from the whole body model, and its impact on computation time and memory evaluated.

In each case, the matrix was first zero-padded to avoid the effects of Fourier ghosting artifacts resulting from circular convolution. This requires a doubling of the matrix size in each dimension to fully avoid all Fourier ghosts (35), which results in a large increase in computation time and memory usage. Since only the portion of the field map within the VOI is of interest, it is sufficient to zero-pad by a lesser amount when using the conventional method. In practice, each dimension can be zero-padded by an amount equaling the length of the model in that dimension minus the distance in that dimension between the VOI and the edge of the model nearest the VOI. This places the Fourier ghost just outside the bounds of the VOI, minimizing the impact on computation time and memory usage. As previously noted, the VOI-based method doubles the matrix size along each dimension as part of its algorithm.

The memory overhead requirement of each method was evaluated by calculating the difference between the measured peak memory usage during computation and the measured memory usage after the computation. This difference represents the extra memory required purely for performing the computation, which is in addition to the amount required to store the input susceptibility and output ΔB data matrices, as well as any other data, programs, or operating system overhead needed. This value is of relevance because the computer must have the full amount of the memory overhead available for the computation to avoid disk swapping, which greatly reduces calculation speed. The memory usage values were measured by tracking the “Memory (Private Working Set)” of the MATLAB executable using the Windows (Microsoft Corporation, Redmond, WA) Task Manager, and each method was implemented as a MATLAB function to ensure that it would free its memory upon completion. The computation time required for each method was measured by enclosing the calls to the respective MATLAB functions with the MATLAB commands “tic” and “toc”, which report execution time in seconds. Each method was run three times and the results averaged. The testing hardware used was a

64-bit Windows workstation with 36 GB of memory and dual hex-core 2.66 GHz Intel (Intel Corporation, Santa Clara, CA) Xeon X5650 processors.

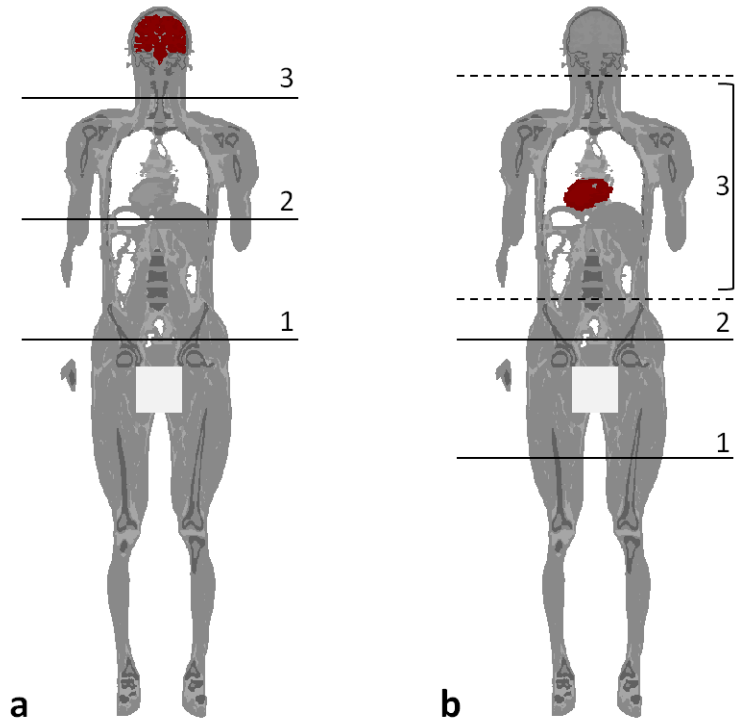

Figure 3.3. The human body models used for numerical evaluation of the ΔB field within the brain and heart VOIs (shown in dark red). For evaluation of the brain, the models used were: the untruncated whole body model, the truncated portions above the waist (1), above the mid-torso (2), and above the neck (3) (a). For evaluation of the heart, the models used were: the untruncated whole body model, the truncated portions above the thighs (1), above the waist (2), and the torso and neck region surrounding the heart (3) (b).

Table 3.1. List of magnetic susceptibility values of anatomical tissue types.

Tissue Type	χ (ppm)	Reference
Bone	−11.31	(38)
Soft tissue/water	−9.04	(19)
Gray matter	−8.97	(19)
White matter	−8.80	(19)
Fat	−7.79	(19)
Blood	−8.47	(19)
Air	0.40	(19)
Lung	4.32	(39)

3.3.3 Application to a Passive Shimming Simulation

The efficacy of the algorithm was further evaluated for use in passive shim optimization applications. Previous work has explored the use of thin sheets of bismuth and zirconium inserted into slots in a cylindrical grid for improved whole-brain shimming in the mouse (18), and it is this upon this design that the simulation experiment is modeled. The previous approach involved experimental acquisition of unit shim responses of the passive shim element B_0 perturbation fields, but noted that it might be beneficial to instead be able to calculate these perturbation fields in simulation. It is this step that has the potential to be accelerated by the proposed method.

A stack of two bismuth (χ = −164 ppm) (1) shim elements of size 3.2×4.6×1.0 mm was placed into the simulated model region at a radial distance of 15.0 mm away from the isocenter of the magnet, as shown in Figure 3.4. The target VOI chosen was a 14.0×14.0×28.0 mm region centered on the isocenter, and the voxel resolution was 0.2 mm isotropic. The resultant ΔB field in the VOI from the susceptibility distribution of the bismuth shim elements was then calculated using the conventional and VOI-based methods and the corresponding computation time and memory requirements were compared. This calculation represents a simulated alternative to the experimental acquisition of a unit shim response as per the previous work. As with the human

body model calculations, the matrix was first cropped and zero-padded just enough to avoid placing a Fourier ghost within the VOI so as to minimize the time and memory used.

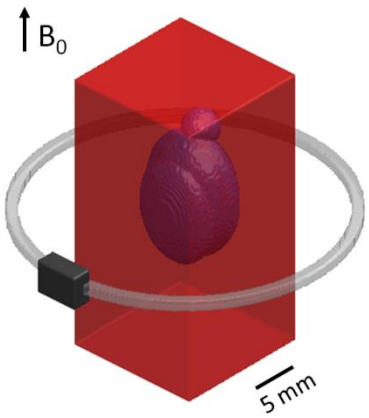

Figure 3.4. A 3D model of the passive shimming calculation setup with the bismuth shim elements (black), the target VOI (light red), and a ring representing the passive shim former. For size comparison, a representative model of a mouse brain (dark blue) is shown within the VOI.

3.4 Results

3.4.1 Phantom Simulation

Figure 3.2 shows the validation results of the phantom simulation experiment. The VOI-based ΔB calculation method produces effectively identical results to the whole-volume method, with a root-mean-square difference in computed ΔB value between the two methods of $3.75 \cdot 10^{-16}$ ppm within the VOI. This level of deviation can be attributed to the limits of precision of the double-precision floating point variables used in the numerical calculations. Similar levels of agreement between the VOI-based and whole-volume methods were observed in all following simulation experiments as well. Note that both Fourier Transform-based calculation methods produce errors at the edges of the sphere as compared to the analytical calculation method due

to discrete quantization effects. This is a well-known inherent limitation of the Fourier Transform-based calculation, and the results match those shown in previous work (12,20,34-36).

3.4.2 Human Body Model Simulation

As shown in Figure 3.5 and Figure 3.6, the partially-truncated body calculations for both the brain and heart VOI yielded significant deviations with respect to the full-body calculation. These deviations are non-linear in spatial distribution and vary primarily in the B_0 direction. The magnitude of the error increases with greater truncation of the human body model. In comparison, the VOI-based calculation yielded effectively zero error for both VOIs as noted above.

Table 3.2 shows the computation time and memory overhead for all the human body model numerical calculation experiments. With the whole-volume method, the computation time and memory overhead both decreased approximately linearly with truncation extent with respect to the whole human body model. The VOI-based method utilized a similar amount of time and memory for calculations of both the heart and the brain, as the source susceptibility region was identical and the sizes of the VOIs were both similar. In this case, the amount of memory overhead was significantly reduced, while the calculation time was comparable to the whole body calculation case using the whole-volume method.

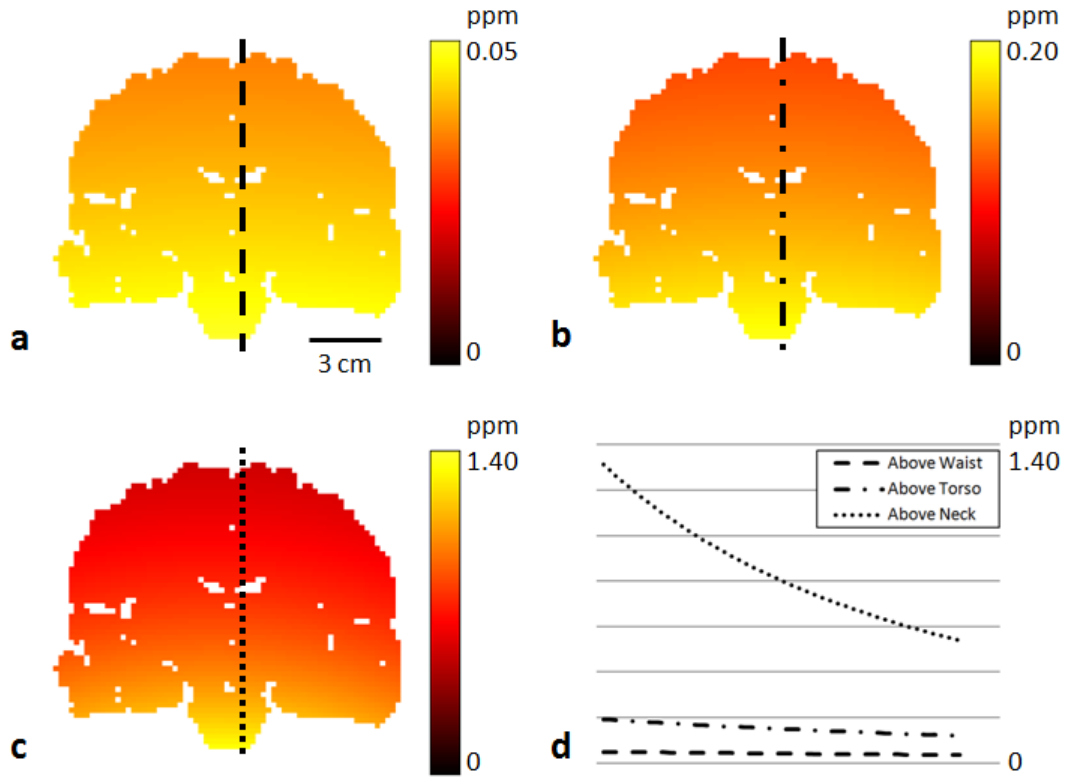

Figure 3.5. The error maps in a representative coronal brain slice of the calculated Δ*B* fields resulting from truncating the portions of the human body model: below the waist (a), below the mid-torso (b), and below the neck (c). The error largely varies in the axial (z) direction as a result of the abrupt boundary condition changes caused by the truncations of the model. Note that each subfigure has a different color scale to highlight the spatial dependence for each case. The absolute changes can be assessed with a line plot (d) along the axial line indicated in each map, from inferior to superior.

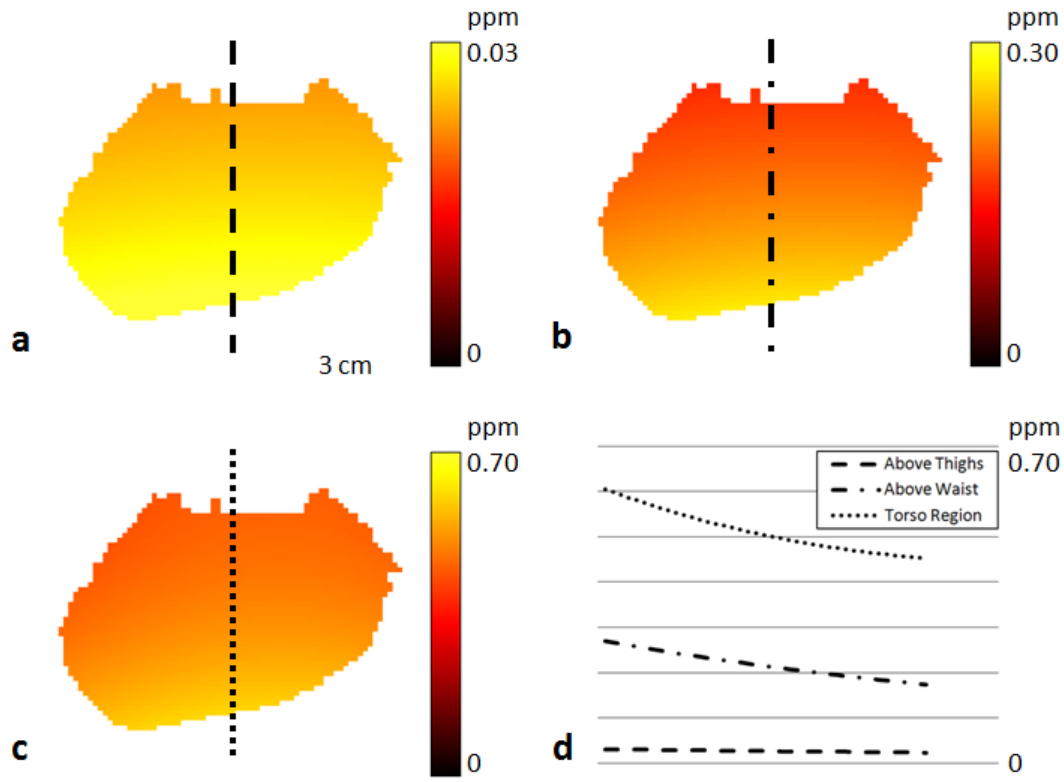

Figure 3.6. The error maps in a representative coronal heart slice of the calculated Δ*B* fields resulting from truncating the portions of the human body model: below the thighs (a), below the waist (b), and above and below the torso (c). The error largely varies in the axial (z) direction as a result of the abrupt boundary condition changes caused by the truncations of the model. Note that each subfigure has a different color scale to highlight the spatial dependence for each case. The absolute changes can be assessed with a line plot (d) along the axial line indicated in each map, from inferior to superior.

Table 3.2. Results of the Duke human body model calculation experiments.

Calculation Method	Body Model	VOI	Memory Overhead (GB)	Computation Time (s)	Mean Error (%)
Conventional	Whole body	Whole body	14.2	53	–
Conventional	Whole body	Brain	10.7	42	0.0
Conventional	Above waist	Brain	4.6	17	3.5
Conventional	Above torso	Brain	2.8	12	12.7
Conventional	Head only	Brain	0.7	3	66.1
VOI-based	Whole body	Brain	0.7	44	0.0
Conventional	Whole body	Heart	8.9	32	0.0
Conventional	Above thighs	Heart	5.1	18	2.0
Conventional	Above waist	Heart	3.6	13	15.7
Conventional	Heart region only	Heart	2.5	9	36.7
VOI-based	Whole body	Heart	0.7	43	0.0

3.4.3 Passive Shimming Simulation

The passive shimming calculation experiment using the conventional method required 1.86 GB of memory overhead and 8.5 s of computation time. The computation using the VOI-based method required 0.24 GB of memory overhead and 4.2 s of computation time. For this application, the proposed method showed a 50% decrease in computation time as well as a marked decrease in memory required for the calculation of a single unit shim B_0 perturbation field response.

3.5 Discussion

The VOI-based ΔB calculation method produces effectively the same results as the full-body calculation with a significant reduction in computer memory requirements. For the high spatial resolution of the *Duke* human body model, the full-body field map calculations required

excessive memory using conventional methods. For such an experiment, the computer would need a minimum of approximately 16 GB of RAM when taking operating system overhead into account, which is generally only installed in high-end workstations. For standard desktops or laptops, such calculations would not be able to be executed using the whole-volume method. In contrast, the VOI-based method can perform these calculations on most modern desktop computers, as shown in Table 3.2. The computation time and memory overhead figures shown are measured from both algorithms executing in an interpreted MATLAB environment; we predict that implementation of the algorithms in a compiled language such as C++ would likely yield proportional speed improvements for both methods, but the respective memory footprints would likely remain the same.

In practice, most numerical experiments target relatively small VOIs while requiring a solution of the entire human body model, which is inefficient. As illustrated, even truncation at the waist produced significant error for the calculation of the ΔB map in the brain. The accuracy of the resultant ΔB map may be inadequate for shim optimization calculations. Similarly, for the heart VOI calculations, the truncation at thigh level produced significant error, and further truncation resulted in much greater error. Both of these truncation cases did reduce memory usage and computation time, but the memory usage overhead for these cases is still high. In contrast, the VOI-based method was able to calculate the ΔB field distribution in the VOIs accurately and in a much more memory-efficient manner. Therefore, the proposed method extends the capability to calculate accurate ΔB field maps from high-resolution human body susceptibility map data to lower-power computer systems, where the maps can then be used for various B_0 artifact correction applications (33,34).

Conversely, one potential limitation of the VOI-based calculation method is that only a small volume of susceptibility source and/or target VOI regions (~25% of the total volume) may be selected if comparable computation time to the conventional method is desired. As more of the total problem space is selected, the speed losses from subdivision of the 3DFFT operations

begin to outweigh the speed gains from the avoidance of processing irrelevant regions of the problem space. Thus, this method is best suited for “sparse” matrices wherein the susceptibility source regions and targeted VOIs may be relatively small and separated by relatively large distances. For human body field calculation applications, the susceptibility source matrix is not sparse enough for the VOI method to yield an increase in computation speed; the method only reduces memory usage. However, for matrices with sufficient sparsity, such as in passive shimming applications, the method can reduce computation time as well. This computation time reduction can have a large impact for repeated, iterative calculations performed during *in vivo* MRI studies in which the time that a human subject can tolerate in the MRI scanner is limited. Thus, the new method can be used to accelerate passive shim design and optimization via the use of computed perturbation fields.

4 *In Vivo* Synergistic Shimming Validation

In this section, the *in vivo* validation experiments that were performed to demonstrate the effectiveness of the synergistic shimming technique will be addressed. The target application was shimming of various regions of the mouse brain, where air-tissue boundaries cause localized static field inhomogeneities that make localized spectroscopy difficult.

4.1 In Vivo Mouse Brain Frontal Lobe Shimming

The first region to be targeted for *in vivo* synergistic shimming was the frontal lobe of the mouse brain. The olfactory bulb in this region is affected by susceptibility-induced inhomogeneities arising from the geometry at the front of the brain, and it would be of interest to researchers to be able to reduce the effects of these inhomogeneities.

4.1.1 Subject Preparation

Each mouse subject used was a normal adult mouse procured in accordance with Institutional Animal Care and Use Committee (IACUC) guidelines. First, the mouse was removed from its cage and placed in a anesthetization box where it was exposed to 2% isoflurane until loss of consciousness. It then received eye drops and was transported to the magnet, where it was placed on the animal bed and positioned using the bite bar as follows. A small piece of foam (axial width = 10 mm) with a hole bored through the center (diameter = 7 mm) was placed between the hard plastic nose cone and the mouse body to avoid friction against the eyes and to avoid B_0 susceptibility artifact in the mouse brain resulting from the nose cone's vertical wall. The mouse's front teeth were hooked onto the bite bar, and then the bite bar was carefully pulled through the foam and nose cone until the mouse head was snug. This placed the center of the mouse brain approximately 15 mm away from the nose cone vertical wall. A respiratory monitor was then attached to the mouse torso with medical tape to ensure that the mouse continues to breathe properly throughout the experiment. The mouse was then

secured in place with medical tape, and a vortex heater used to supply heated air through a tube in the animal bed to keep the sedated subject warm.

After this point, the shim frame could be slid over the mouse and animal bed and secured in position, with the anesthesia and respiratory monitor tubes exiting through a notch cut in the rear of the frame's main tube. The mouse respiration was observed to remain stable and normal at around 30 breaths per minute. An example photograph of the shim frame in use is shown in Figure 4.1.

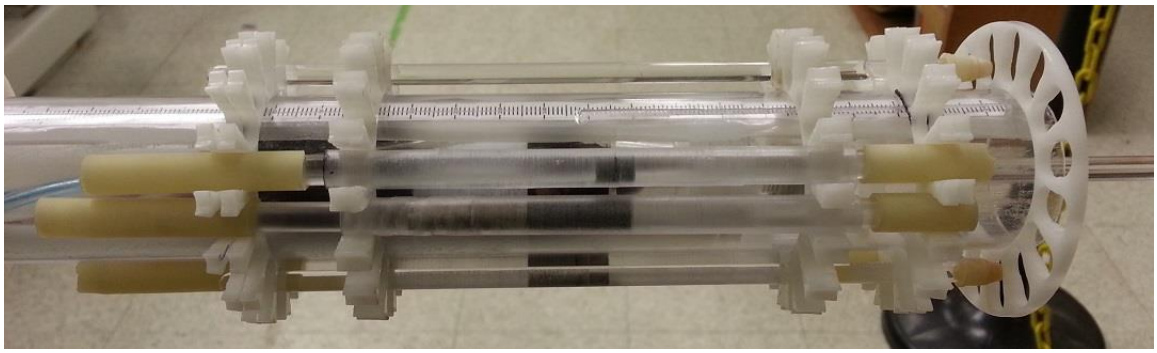

Figure 4.1. Photograph of the shim frame in use. Note the presence of the fiducial cylinders (top and bottom), the z fiducial marker (top-middle), and shim elements (middle-bottom, and rear), as well as the anesthesia and respiratory monitor (left, blue) tubes running down the inside of the shim frame.

4.1.2 Acquisition Procedures

The mouse, with the shim frame, calibration rods, and fiducial marker mounted in place (as described in Chapter 2), was inserted into the bore of the Bruker 7T animal magnet such that the center of its brain lay on the isocenter of the magnet. A tripilot scan was used to ensure proper positioning of the mouse.

The linear active shims were then disabled (set to zero current), and a B_0 field inhomogeneity map was acquired using the standard Bruker FieldMap sequence. The first echo time (TE) for this sequence was set to 2.90 ms (at least minimum TE + 3 × gradient rise time)

after the excitation pulse to avoid acquisition during eddy currents in accordance with the scanner documentation. The second echo was acquired at 7.66 ms in accordance with the fat-water in-phase condition. The number of averages was set to 1 and the TR was set to 18 ms, higher than the minimum, to improve signal to noise ratio while keeping the total scan time tolerable for the subject. The FOV was 44.8 mm × 44.8 mm × 44.8 mm with a 128×128×128 matrix size, or a 0.35 mm/vx isotropic resolution. The excitation pulse used was a bp pulse with 50 μs duration and 25.6 kHz bandwidth. The effective spectral bandwidth of the sequence was set to 50 kHz to avoid a zipper artifact that was otherwise observed to run along the center line in the axial direction.

This initial field map represents the baseline case without any shimming. A cubic volume of interest (VOI) encompassing the front of the brain was then chosen, and this initial map was input together with the VOI into MapShim, the standard Bruker B_0 field map-based localized shimming solution. The first-order linear active shims and the second-order Z2 active shim were adjusted by MapShim for optimal local B_0 field homogeneity, and a second FieldMap was acquired. This map represents the case in which industry-standard localized shimming provided by the vendor was used.

The initial field map and VOI were then input into the synergistic optimization software and an improved synergistic shimming solution consisting of four passive shim elements (as shown in Figure 4.2) and linear active shim settings was found. The shim elements were mounted on the shim frame in the positions specified by the software. The active shim coil currents were set in accordance with the synergistic shimming solution, and third and final B_0 field map acquired. This map represents the synergistic shimming case.

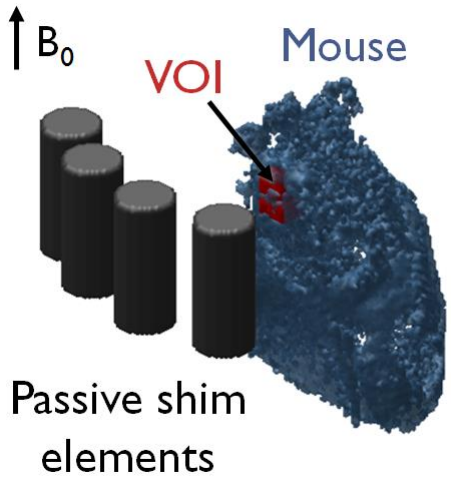

Figure 4.2. 3D rendering of the frontal lobe experiment VOI passive shim configuration.

4.1.3 Results

A single mouse subject was processed as per the above procedures and with the resulting passive shim configuration shown in Figure 4.2. The B_0 field inhomogeneity maps were compared to assess the improvement in shimming quality of the synergistic shimming system versus first-order active shimming alone. As shown in Figure 4.3, synergistic shimming results in markedly lower inhomogeneities near the front edge of the VOI. Quantitatively, there was a reduction in variance of ΔB_0 values of the voxels within the VOI from 7.3206 to 5.4426, or a reduction of 25.6%, across the whole VOI.

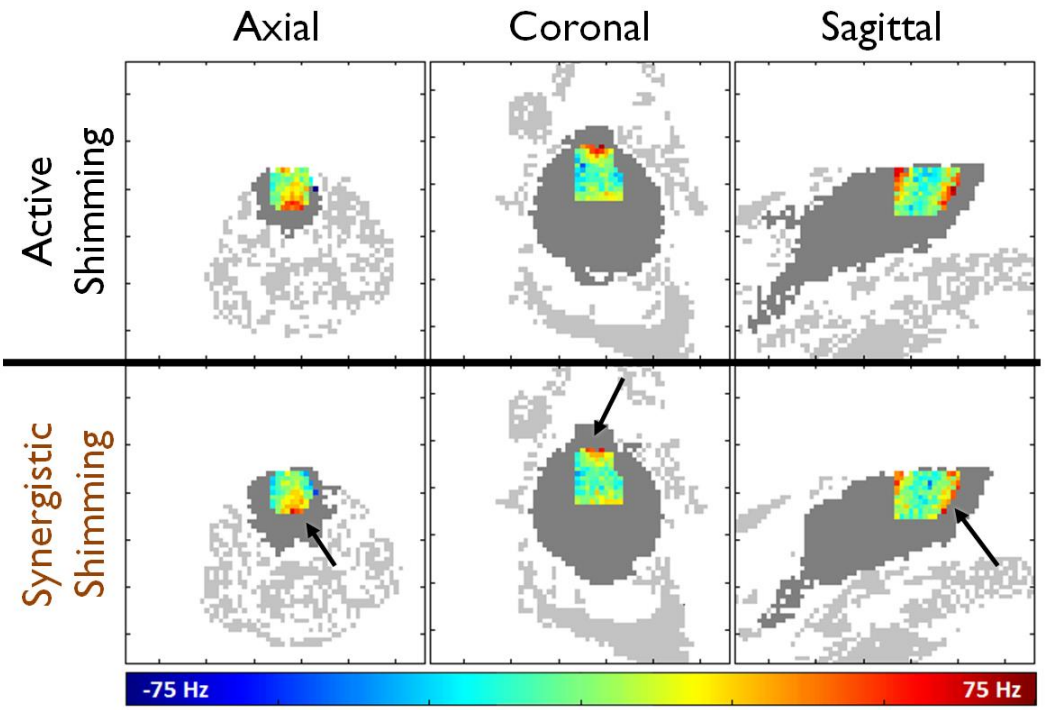

Figure 4.3. Visual comparison of linear active shimming vs. synergistic shimming in the frontal lobe.

4.2 In Vivo Mouse Brain Temporal Lobe Shimming

For the next test of the synergistic shimming system, we chose the temporal lobe. The proximity of the temporal lobe to the air pockets of the posterior maxillary sinuses presents additional shimming challenges.

4.2.1 Acquisition Procedures

The subject preparation and acquisition protocols were the same as before, but with the addition of acquiring MR water peak spectra in each case. The VOI chosen was a 2.1 mm × 2.1 mm × 2.1 mm cube in the brain region above the right ear canal as it passes under the brain, representing an MR spectroscopy voxel of reasonable size for mouse studies. The acquisition was a standard PRESS sequence without water suppression so as to see the water peak line

width (TE = 20 ms, TR = 2500 ms, TE_1 = TE_2 = 10 ms, number of averages = 32, N = 4096, spectral width = 3333.33 Hz, dwell time = 150 μs). The standard Bruker CalcLineWidth macro was then used to computer the full-width half-maximum (FWHM) and full-width 10%-maximum values for each acquired water peak.

4.2.2 Results

A single mouse subject was processed as per the above procedures. Representative slices of the B_0 field inhomogeneity maps for the whole-volume magnet autoshim, localized active shimming via MapShim, and localized synergistic shimming cases are shown in Figure 4.4. The VOI is indicated by the black outline. A detailed view of this VOI is shown in Figure 4.5. It can be seen in the autoshim field maps that there is a strong field gradient arising from the boundary between the air-filled sinus cavity and the brain tissue. This inhomogeneity is partially compensated by the linear and Z2 active shims in the localized active shimming field map. However, major fluctuations remain, as the inhomogeneity is not merely first-order in nature and thus able to be adequately compensated by these active shim coils alone. MapShim was not able to optimize the remaining second-order active shims because the required currents were significantly higher than the system maximums. In contrast, the synergistic shimming algorithm was able to find a combination of passive shim elements and active shim settings that was able to further reduce the inhomogeneity. A quantitative evaluation of this reduction is shown in Table 4.1. The synergistic shimming solution reduced variance in the VOI over localized active shimming by 11.4%.

Table 4.1. ΔB_0 variance within the temporal lobe VOI for whole-volume shimming, localized active shimming, and localized synergistic shimming. Synergistic shimming reduced ΔB_0 variance in the VOI over localized active shimming by 11.4%.

Case	Variance	Percent Change
Whole-volume Autoshim	6.1373	–
Localized Active Shim	5.0088	−18.4%
Localized Synergistic Shim	4.4384	−27.7%

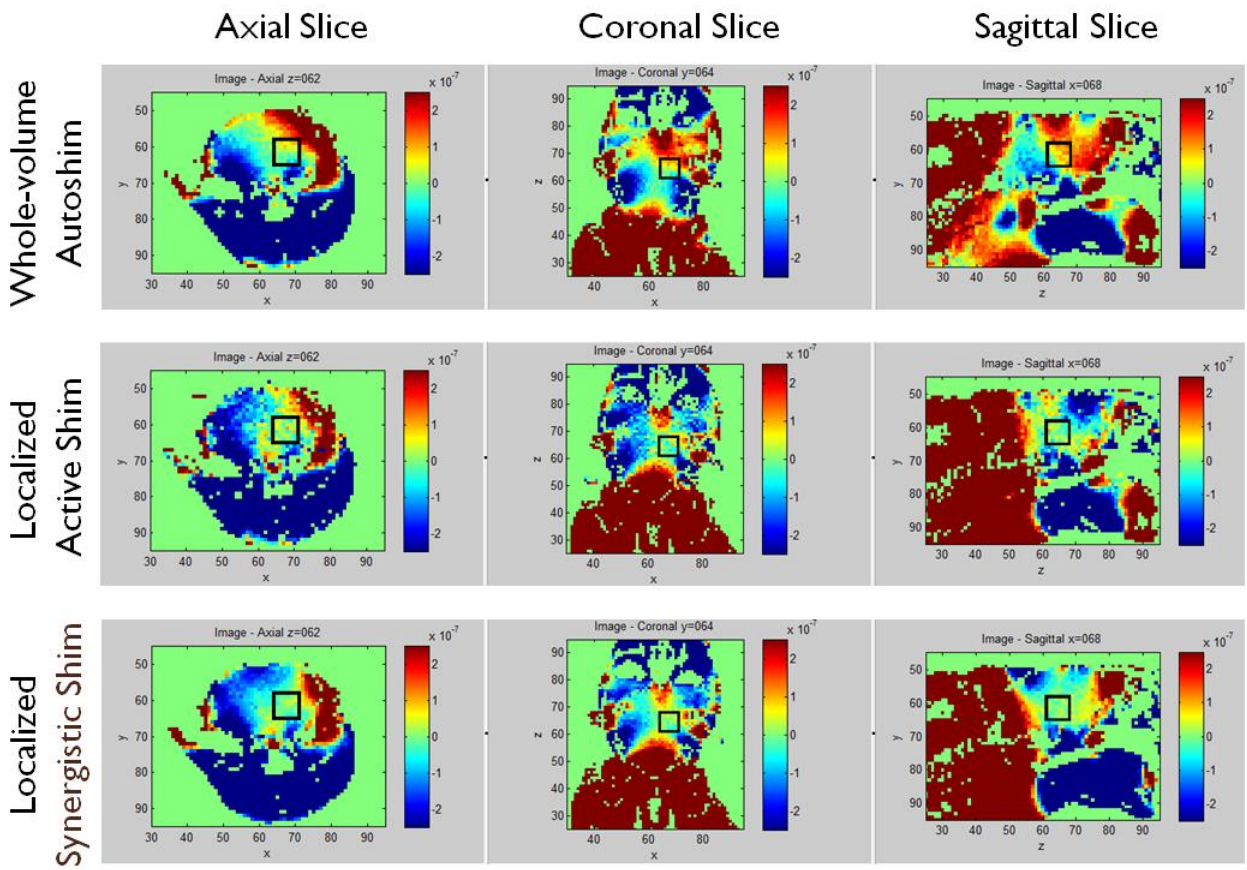

Figure 4.4. B_0 inhomogeneity maps for the temporal lobe VOI. The VOI is indicated by black outline. The color scale has bounds of ±0.25 ppm (±75 Hz).

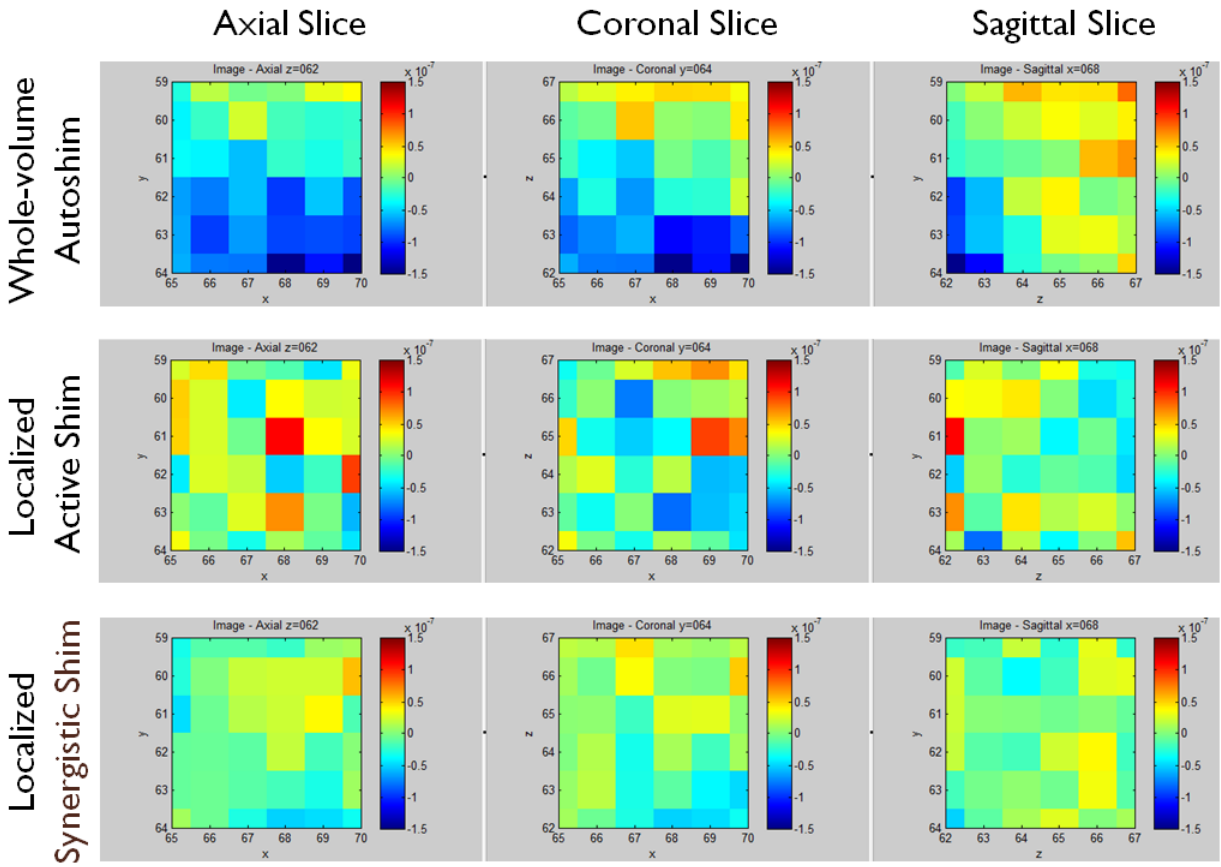

Figure 4.5. Close-up of the B_0 inhomogeneity maps for the temporal lobe VOI. The VOI is indicated by black outline. The color scale has bounds of ±0.15 ppm (±45 Hz).

Histograms of the B_0 field map values within the VOI and the corresponding MR spectroscopy water peaks further demonstrate this reduction in B_0 inhomogeneity, as shown in Figure 4.6. The region occupied by the spectroscopy voxel, being 2.1 mm × 2.1 mm × 2.1 mm, contains 216 individual 0.35 mm × 0.35 mm × 0.35 mm field map voxels, and it is these individual ΔB_0 values at each of these field map voxels that are plotted in the histograms shown. The ideal histogram and water peak shape would be effectively a Dirac delta function, indicating perfect B_0 field homogeneity and perfectly homogenous resonance frequencies for all hydrogen nuclei within the spectroscopy voxel. The further the deviation from this shape, the greater the level of inhomogeneity in static magnetic field and resonance frequency. Standard localized active shimming appears to not significantly improve the histogram shape, whereas synergistic

shimming noticeably makes the histogram taller and narrower. The improvement in MRS water peak is not as dramatic, with the peak largely staying the same but the tails smoothening and lowering. This is reflected in the quantitative data in Table 4.2; the peak's full-width half-maximum (FWHM) value is not improved, but the full-width 10% maximum value is reduced by 39.7%.

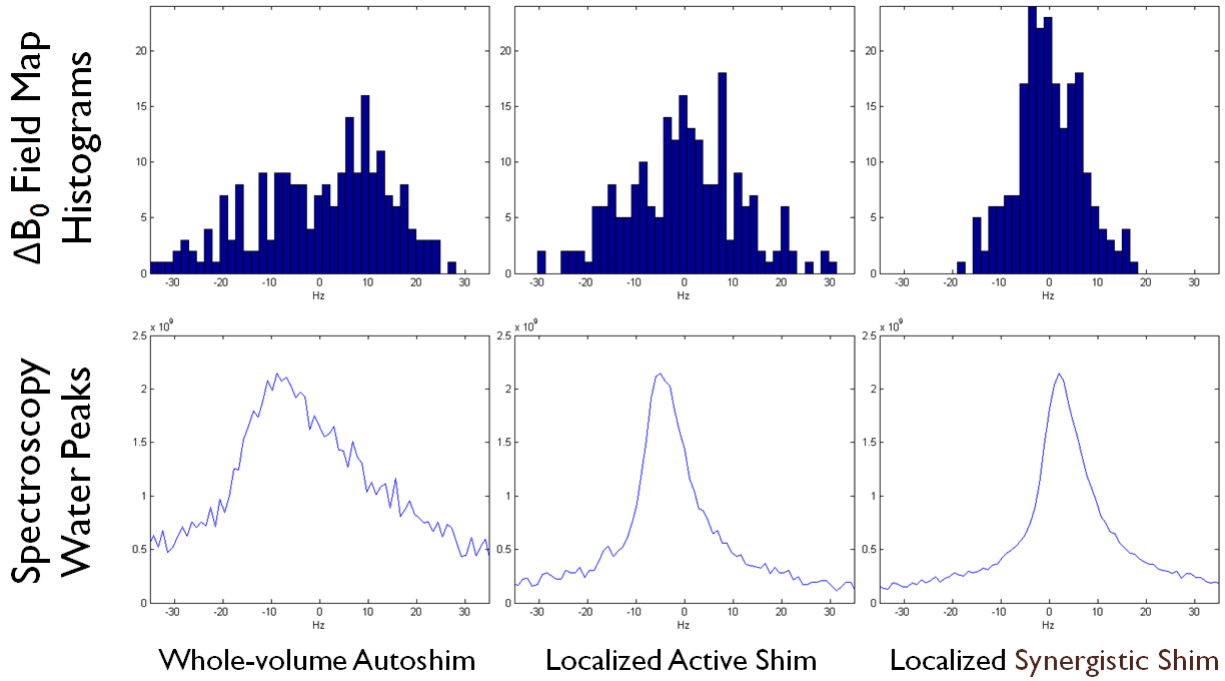

Figure 4.6. ΔB_0 histograms and MRS water peaks for the temporal lobe VOI.

These results suggest that even for this difficult region, synergistic shimming has potential for improving the local B_0 field homogeneity for *in vivo* MR spectroscopy studies. The water peak FWHM remained the same, suggesting that differentiation of close chemical species might not be improved, but the improvement in the tails of the water peak suggests that synergistic shimming may improve the quantification of metabolites with low concentrations and thus low signal levels.

Table 4.2. MRS water peak FWHM and 10% maximum values for the temporal lobe VOI for whole-volume shimming, localized active shimming, and localized synergistic shimming. Synergistic shimming reduced the full-width 10%-maximum for the VOI over localized active shimming by 39.7%.

Case	Full-width Half-maximum (FWHM) (Hz)	% Change	Full-width 10%-maximum (Hz)	% Change
Whole-volume Autoshim	32.3	–	1980.7	–
Localized Active Shim	12.7	−60.7%	56.7	−97.1%
Localized Synergistic Shim	12.7	−60.7%	34.2	−98.3%

4.3 Discussion

We have demonstrated the ability to use the synergistic shim system to improve ΔB_0 homogeneity within targeted VOIs in the frontal and temporal lobe of *in vivo* mice, with reductions in variance within the VOI of 25% and 11% and reductions in water peak full-width 10%-maximum values of 39%. This demonstrates that the system as a whole works in multiple target regions and suggests that it may be useful to improve ΔB_0 homogeneity for targeted spectroscopy applications in general.

As the next step after these pilot studies, we wanted to further quantify the limits of the synergistic shim method via analysis of multiple VOIs in a cohort of *in vivo* mouse subjects and thereby definitively characterize brain regions where the method could enable research previously hindered by B_0 inhomogeneity issues. We also wanted to acquire *in vivo* MRS spectra as a further demonstration of the improved shim.

The MRS protocol developed for this purpose was a PRESS sequence similar to the basic one used for line width determination (TE = 7.842 ms, TR = 2500 ms, TE_1 = 4.70 ms, TE_2 = 3.14 ms, N = 1024, spectral width = 4166.67 Hz, dwell time = 120 μs). An unsuppressed water reference with 32 averages and a VAPOR (bandwidth = 250 Hz) water-suppressed spectrum

with 128 averages were acquired. Several of these parameters, notably the TE, number of points, and number of averages, were changed from the previous protocol improve the SNR. Outer volume suppression was also enabled. The spectroscopy voxel used was initially 2.1 mm × 2.1 mm × 2.1 mm, and later expanded to 3.0 mm × 3.0 mm × 3.0 mm.

In order to demonstrate an improvement in MRS spectra, it would be necessary to achieve a reasonable localized shim with active shimming alone, acquire an MRS spectrum, then perform synergistic shimming, acquire a second spectrum, and compare the quality of the two spectra. To systematically demonstrate this across multiple *in vivo* subjects, it would be necessary to define a representative VOI that can be targeted across subjects. For example, our plan was to define the location of the target VOI as being a certain distance away from the bregma in the axial/head-foot direction and a certain percentage of the brain height and width away from the brain edge in the anterior-posterior and left-right directions, respectively.

However, due to the relative weakness of our magnet's shim coils and the relative difficulty of the shim problem of the mouse brain, the standard MapShim localized active shimming method often failed to reliably find a combination of shim currents that could adequately shim the target VOI, across a multitude of target VOIs, even at the most lenient available setting (optimizing only the linear and Z2 shim currents). This made establishing a consistent, well-defined VOI that could be adequately shimmed and targeted across subjects impossible. Additionally, the poor shim combined with relatively poor signal-to-noise ratio (SNR) from our 72 mm radiofrequency (RF) transmit-receive volume coil resulted in extremely poor *in vivo* spectra even in the best case despite reasonable water suppression, as shown in Figure 4.7. Neither analysis with Bruker Topspin software nor LCModel (40) were able to identify or quantify individual metabolites. This could potentially be ameliorated by using a smaller volume coil or surface coil that could deliver better SNR, but the shim frame hardware would need to be heavily redesigned to fit around these coils, and there was not sufficient time to do so. Choosing a larger VOI (3.0 mm × 3.0 mm × 3.0 mm, perhaps inappropriate for localized mouse

spectroscopy) also improved SNR, but the reliability of the shimming remained an issue. In theory, with better shim coil and RF coil performance, it should be possible to demonstrate improved MRS spectrum acquisition for the synergistic shimming method, based on the improvement in *in vivo* mouse brain B_0 field homogeneity and water peak shape. Unfortunately, both the shim performance and RF coil performance had degraded over time due to various technical issues. Without a stable baseline for comparison, it was thus not possible to demonstrate comparative improvement in MRS, and methods to bypass these limitations were not able to be fully explored due to time constraints.

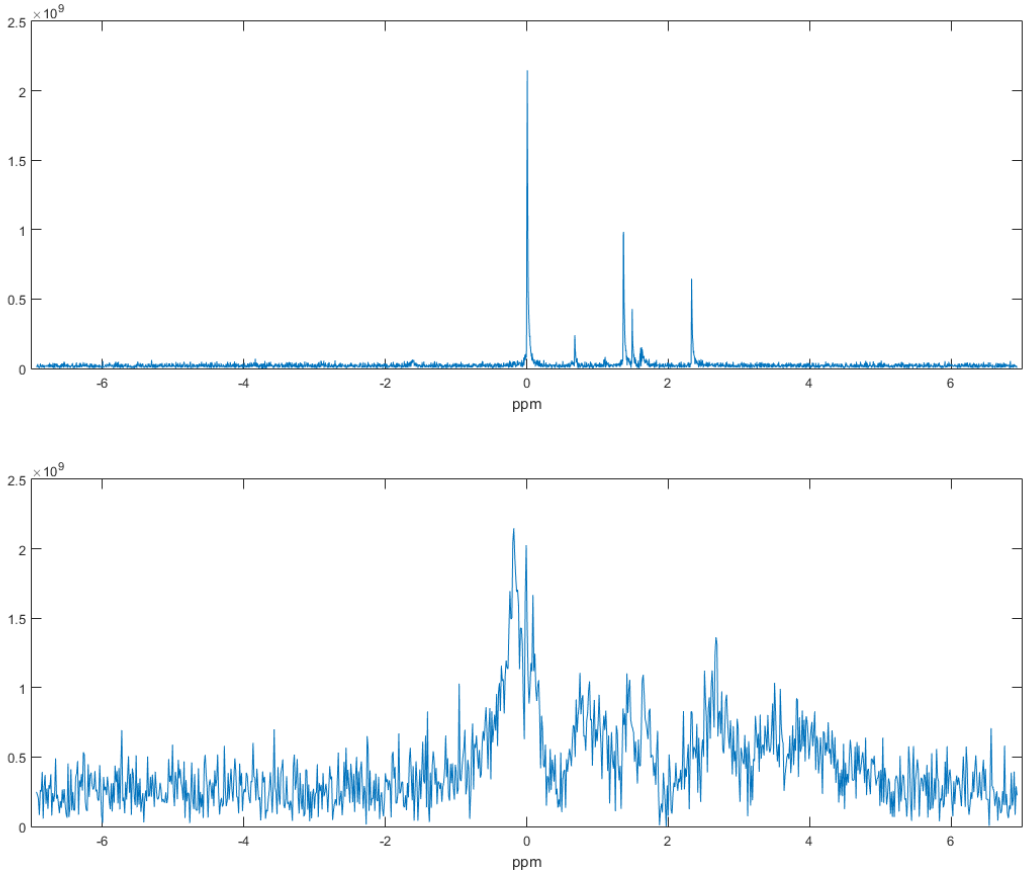

Figure 4.7. MR spectra acquired from an NAA-choline-creatine phantom (top) and *in vivo* mouse (bottom). The spectrum quality was insufficient for metabolite quantification.

5 Conclusions

This research resulted in a proof-of-concept synergistic passive shimming system that can be used to improve B_0 field inhomogeneity for high-field (7T) MR imaging studies of the mouse brain. In theory, this should allow for more effective imaging artifact reduction and improved MRS peaks in brain regions near air-tissue interfaces. It is expected that this system will be able to be extended to other applications, such as *in vivo* studies of the human brain at high field. The novel VOI-based Fourier Transform method created in the course of the synergistic shimming system development is itself a significant contribution to the field. Its ability to efficiently compute passive shim perturbation fields and whole-body B_0 homogeneity maps has applications for improving or enabling other potential passive or active shimming methodologies.

5.1.1 Potential Improvements

The initial B_0 map acquisition, optimization, and shim element placement can be performed within 20 minutes or less using a modern multi-core workstation, which should be adequate for most animal studies. Further speed improvement in the system pipeline may be necessary for human studies; for example, the computation time might be offset by performing the computation while anatomical scans are being acquired.

The system can also be improved in other ways; for example, in the current system, it is necessary to remove the subject from the magnet to readjust the passive shim elements. A more complicated design that allows for passive shim element adjustment while the subject is inside the magnet may be desirable for improved patient comfort and ease of operation.

Another avenue of improvement is the development of a more sophisticated cost function. In its current form, the method typically worsens field homogeneity in regions outside the VOI. If the whole brain is chosen as the VOI, the method typically would not be able to find a passive shim set that can improve whole brain homogeneity at once. If a more sophisticated

cost function is developed, which concentrates on improving homogeneity within the VOI but also makes sure not to disrupt the homogeneity in brain regions outside the VOI too much, it is possible that standard imaging or even whole-brain shimming could be performed with the synergistic shim system in use. This may also require more flexibility in placement of passive shim elements.

5.1.2 Challenges

Hardware performance and time constraints resulted in the system being unable to be validated more thoroughly using a cohort of mice subjects. One avenue that was explored to ameliorate the hardware performance issues was to improve the magnet's active shims by mapping and optimizing the second-order active shims ourselves in addition to the first-order active shims rather than relying on Bruker's proprietary MapShim methods. To this end, the Bruker shim calibration files and specifications were read into MATLAB to create simulated active shim coils that could be used to compute optimal active shims for the target VOI. Briefly, active shim coil characterization data was acquired by acquiring a standard B_0 field map of a basic water phantom with a single active shim coil manually set to a fixed current (e.g. 20% of the maximum) while all other shim currents remain at zero. Then, if the single shim coil's current is also set to zero, and the resulting B_0 field map subtracted from the first field map, the result is a difference map showing the B_0 perturbation field of the single active shim coil. As the strength of the perturbation field produced by the shim coil is approximately linearly proportional to the current within the coil, this difference map is sufficient to characterize the associated shim coil and thus create a simulated active shim coil that matches well with the real-world shim coil. Unfortunately, the specifications, shim calibration files, and acquired test data all appeared to be inconsistent with one another. It was presumed that Bruker used proprietary methods to achieve their shims, and as Bruker was not willing to reveal these, it was not possible to map computed second-order active shim settings with system shim settings and thus implement this approach.

5.2 Future Directions

5.2.1 Adaptation to Human Brain Shimming

In order to adapt the synergistic shim system for human brain shimming, some exploratory simulations and changes in the design may be required. For example, larger shim elements of greater radius would likely be required, and the frame may need to be hemispherical to account for the limited space within a typical human magnet bore setup. Additionally, it may be beneficial to design the frame around the assumption that the subject holds their head in a particular position; for example, it may be beneficial for the shim problem for the subject to tilt their head backwards in the scanner to shift the sinus artifact out of the frontal lobe (6). The optimal range of parameters to search may vary based on this starting assumption.

5.2.2 Hardware Integration

One important advantage of the synergistic shim system is that, excluding the computer workstation, the hardware costs are low, as the plastics, tubing, and graphite and titanium rods are all widely available and inexpensive. This makes such a system more accessible than high-performance active shimming systems that can cost tens to hundreds of thousands of US dollars. The system is thus potentially appealing as an economical way to retrofit older magnets with better shimming technology. There is also potential for integrating such a system into experimental low-cost magnet designs such as the recently proposed design for a gradient-less, portable, rotating MRI scanner (41).

Alternately, a current topic of great interest in the MR community is the development of next-generation shimming and RF coil hardware that can handle the higher B_0 and B_1 field homogeneity demands of high-field imaging (7 T and above). Various proposals have been made involving developing comprehensive hardware packages that combine the multichannel RF coil array with high dielectric constant materials (HDM) (42) or dynamic localized active shim

coil sets (43). It is possible that optimized passive shimming or synergistic passive and active shimming might have a role to play in such next-generation hardware. For example, passive shim placement might be optimized in simulation to compensate for strong gradients that the localized active shim coils might not be able to handle given their geometries and maximum shim currents. Alternately, lower-cost RF arrays that omit localized active shims and their amplifier hardware might greatly benefit from the inclusion of synergistic passive shims for B_0 and HDM for B_1.

Bibliography

1. Schenck JF. The role of magnetic susceptibility in magnetic resonance imaging: MRI magnetic compatibility of the first and second kinds. Med Phys 1996;23(6):815-850.

2. Cusack R, Russell B, Cox SM, De Panfilis C, Schwarzbauer C, Ansorge R. An evaluation of the use of passive shimming to improve frontal sensitivity in fMRI. Neuroimage 2005;24(1):82-91.

3. Juchem C, Muller-Bierl B, Schick F, Logothetis NK, Pfeuffer J. Combined passive and active shimming for in vivo MR spectroscopy at high magnetic fields. J Magn Reson 2006;183(2):278-289.

4. Dietrich O, Reiser MF, Schoenberg SO. Artifacts in 3-T MRI: physical background and reduction strategies. Eur J Radiol 2008;65(1):29-35.

5. Larvaron P, Bielicki G, Boespflug-Tanguy O, Renou J-P. Proton MRS of early post-natal mouse brain modifications in vivo. NMR in Biomedicine 2006;19(2):180-187.

6. Tyszka JM, Mamelak AN. Quantification of B0 homogeneity variation with head pitch by registered three-dimensional field mapping. J Magn Reson 2002;159(2):213-218.

7. de Graaf RA. In Vivo NMR Spectroscopy: Principles and Techniques. West Sussex, England: John Wiley & Sons, Ltd; 2007.

8. Windischberger C, Robinson S, Rauscher A, Barth M, Moser E. Robust field map generation using a triple-echo acquisition. J Magn Reson Imaging 2004;20(4):730-734.

9. Robinson S, Schodl H, Trattnig S. A method for unwrapping highly wrapped multi-echo phase images at very high field: UMPIRE. Magn Reson Med 2014;72(1):80-92.

10. Jenkinson M. Fast, automated, N-dimensional phase-unwrapping algorithm. Magn Reson Med 2003;49(1):193-197.

11. Kong X, Zhu M, Xia L, Wang Q, Li Y, Zhu X, Liu F, Crozier S. Passive shimming of a superconducting magnet using the L1-norm regularized least square algorithm. J Magn Reson 2016;263:122-125.

12. Salomir R, De Senneville BD, Moonen CTW. A fast calculation method for magnetic field inhomogeneity due to an arbitrary distribution of bulk susceptibility. Concept Magn Reson B 2003;19B(1):26-34.

13. Yang QX, Williams GD, Demeure RJ, Mosher TJ, Smith MB. Removal of local field gradient artifacts in T2*-weighted images at high fields by gradient-echo slice excitation profile imaging. Magn Reson Med 1998;39(3):402-409.

14. Xiang QS, Ye FQ. Correction for geometric distortion and N/2 ghosting in EPI by phase labeling for additional coordinate encoding (PLACE). Magn Reson Med 2007;57(4):731-741.

15. Fernández-Seara MA, Wehrli FW. Postprocessing technique to correct for background gradients in image-based R*(2) measurements. Magn Reson Med 2000;44(3):358-366.

16. Yang X, Sammet S, Schmalbrock P, Knopp MV. Postprocessing correction for distortions in T2* decay caused by quadratic cross-slice B0 inhomogeneity. Magn Reson Med 2010;63(5):1258-1268.

17. Yip CY, Fessler JA, Noll DC. Advanced three-dimensional tailored RF pulse for signal recovery in T2*-weighted functional magnetic resonance imaging. Magn Reson Med 2006;56(5):1050-1059.

18. Koch KM, Brown PB, Rothman DL, de Graaf RA. Sample-specific diamagnetic and paramagnetic passive shimming. J Magn Reson 2006;182(1):66-74.

19. Collins CM, Yang B, Yang QX, Smith MB. Numerical calculations of the static magnetic field in three-dimensional multi-tissue models of the human head. Magn Reson Imaging 2002;20(5):413-424.

20. Cheng YC, Neelavalli J, Haacke EM. Limitations of calculating field distributions and magnetic susceptibilities in MRI using a Fourier based method. Phys Med Biol 2009;54(5):1169-1189.

21. Wilson JL, Jezzard P. Utilization of an intra-oral diamagnetic passive shim in functional MRI of the inferior frontal cortex. Magn Reson Med 2003;50(5):1089-1094.

22. Yang S, Kim H, Ghim MO, Lee BU, Kim DH. Local in vivo shimming using adaptive passive shim positioning. Magn Reson Imaging 2011;29(3):401-407.

23. Juchem C, Brown PB, Nixon TW, McIntyre S, Rothman DL, de Graaf RA. Multicoil shimming of the mouse brain. Magn Reson Med 2011;66(3):893-900.

24. Juchem C, Herman P, Sanganahalli BG, Brown PB, McIntyre S, Nixon TW, Green D, Hyder F, de Graaf RA. DYNAmic Multi-coIl TEchnique (DYNAMITE) shimming of the rat brain at 11.7 T. NMR Biomed 2014;27(8):897-906.

25. Juchem C, Umesh Rudrapatna S, Nixon TW, de Graaf RA. Dynamic multi-coil technique (DYNAMITE) shimming for echo-planar imaging of the human brain at 7 Tesla. Neuroimage 2015;105:462-472.

26. Dewal RP, Yang QX. Volume of interest-based fourier transform method for calculation of static magnetic field maps from susceptibility distributions. Magn Reson Med 2015.

27. Cao Z, Dewal R, Kao C-P, Sica CT, Collins CM, Yang QX. Optimization of static field homogeneity in human brain using combined passive and active shimming. 2010; Stockholm. p 1544.

28. Wen-Jun Z, Xiao-Feng X. DEPSO: Hybrid Particle Swarm with Differential Evolution Operator. 2003 5-8 Oct. 2003. p 3816-3821 vol.3814.

29. Priest AN, De Vita E, Thomas DL, Ordidge RJ. EPI distortion correction from a simultaneously acquired distortion map using TRAIL. J Magn Reson Imaging 2006;23(4):597-603.

30. Clare S, Evans J, Jezzard P. Requirements for room temperature shimming of the human brain. Magn Reson Med 2006;55(1):210-214.

31. Juchem C, Nixon TW, McIntyre S, Boer VO, Rothman DL, de Graaf RA. Dynamic multi-coil shimming of the human brain at 7 T. J Magn Reson 2011;212(2):280-288.

32. Yang S, Kim H, Ghim MO, Lee BU, Kim DH. Local in vivo shimming using adaptive passive shim positioning. Magn Reson Imaging 2011;29(3):401-407.

33. Lee SK, Hancu I. Patient-to-patient variation of susceptibility-induced B(0) field in bilateral breast MRI. J Magn Reson Imaging 2012;36(4):873-880.

34. Koch KM, Papademetris X, Rothman DL, de Graaf RA. Rapid calculations of susceptibility-induced magnetostatic field perturbations for in vivo magnetic resonance. Phys Med Biol 2006;51(24):6381-6402.

35. Jenkinson M, Wilson JL, Jezzard P. Perturbation method for magnetic field calculations of nonconductive objects. Magn Reson Med 2004;52(3):471-477.

36. Marques JP, Bowtell R. Application of a Fourier-based method for rapid calculation of field inhomogeneity due to spatial variation of magnetic susceptibility. Concept Magn Reson B 2005;25B(1):65-78.

37. Dewal RP, Yang QX. VOI-based Fourier Transform method for rapid partial calculation of B(0) maps from sparse susceptibility distributions. 2013; Salt Lake City, UT, USA. p 3773.

38. Hopkins JA, Wehrli FW. Magnetic susceptibility measurement of insoluble solids by NMR: magnetic susceptibility of bone. Magn Reson Med 1997;37(4):494-500.

39. Maril N, Collins CM, Greenman RL, Lenkinski RE. Strategies for shimming the breast. Magn Reson Med 2005;54(5):1139-1145.

40. Provencher SW. Estimation of metabolite concentrations from localized in vivo proton NMR spectra. Magn Reson Med 1993;30(6):672-679.

41. Cooley CZ, Stockmann JP, Armstrong BD, Sarracanie M, Lev MH, Rosen MS, Wald LL. Two-dimensional imaging in a lightweight portable MRI scanner without gradient coils. Magn Reson Med 2015;73(2):872-883.

42. Aussenhofer SA, Webb AG. An eight-channel transmit/receive array of TE01 mode high permittivity ceramic resonators for human imaging at 7T. J Magn Reson 2014;243:122-129.

43. Stockmann JP, Witzel T, Keil B, Polimeni JR, Mareyam A, LaPierre C, Setsompop K, Wald LL. A 32-channel combined RF and B0 shim array for 3T brain imaging. Magn Reson Med 2016;75(1):441-451.

Curriculum Vitae

Rahul P. Dewal

Education

2008 – 2016 **Ph.D.**, Bioengineering, Pennsylvania State University, Hershey, PA

2004 – 2008 **B.S.**, Biomedical Engineering, Electrical and Computer Engineering, Duke University, Durham, NC

Research Experience

2008 – 2016 **Graduate Researcher**, Center for NMR Research, Advisor: Dr. Qing X. Yang

2007 – 2008 **Pratt Undergraduate Research Fellow**, Duke Biomedical Engineering, Advisor: Dr. Patrick D. Wolf

Scholarships and Awards

2011 Leighton Riess Graduate Fellowship

2008 – 2009 Graduate Research Fellowship

2007 – 2008 Pratt Engineering Undergraduate Research Fellowship

2004 – 2008 AT&T Academic Award Scholarship

Selected Presentations and Publications

Dewal RP, Yang QX. Volume of interest-based Fourier transform method for calculation of static magnetic field maps from susceptibility distributions. *Magn Reson Med*. 2015 Jul 3. doi:10.1002/mrm.25747.

Meadowcroft MD, Peters DG, **Dewal RP**, Connor JR, Yang QX. The effect of iron in MRI and transverse relaxation of amyloid-beta plaques in Alzheimer's disease. *NMR Biomed.* 2015 Mar;28(3):297-305.

Dewal RP, Cao Z, Rupprecht S, Yang QX. Realization of a synergistic passive and active shimming system to optimize B_0 field homogeneity in micro MR imaging. 22nd Annual Meeting of the ISMRM, Milan, Italy. May 2014.